J. Fluid Mech. (2012), *vol.* 698, *pp.* 374–405. © Cambridge University Press 2012
doi:10.1017/jfm.2012.96

A new model of roll waves: comparison with Brock's experiments

G. L. Richard and S. L. Gavrilyuk†

Aix-Marseille University, UMR CNRS 6595, IUSTI, 5 rue E. Fermi, 13453 Marseille CEDEX 13, France

(Received 10 August 2011; revised 26 January 2012; accepted 13 February 2012;
first published online 11 April 2012)

We derive a mathematical model of shear flows of shallow water down an inclined plane. The non-dissipative part of the model is obtained by averaging the incompressible Euler equations over the fluid depth. The averaged equations are simplified in the case of weakly sheared flows. They are reminiscent of the compressible non-isentropic Euler equations where the flow enstrophy plays the role of entropy. Two types of enstrophies are distinguished: a small-scale enstrophy generated near the wall, and a large-scale enstrophy corresponding to the flow in the roller region near the free surface. The dissipation is then added in accordance with basic physical principles. The model is hyperbolic, the corresponding 'sound velocity' depends on the flow enstrophies. Periodic stationary solutions to this model describing roll waves were obtained. The solutions are in good agreement with the experimental profiles of roll waves measured in Brock's experiments. In particular, the height of the vertical front of the waves, the shock thickness and the wave amplitude are well captured by the model.

Key words: channel flow, shallow water flows, shear waves

1. Introduction

Uniform fluid flows with a free surface down an inclined plane can be unstable under some circumstances: the flow transforms into a periodic system of hydraulic jumps separated by smooth profiles usually called 'roll waves'. This paper is devoted to the study of turbulent roll waves, i.e. the roll waves appearing in flows with Reynolds number in the range 10^4–10^5. The corresponding periodic waves arising at low Reynolds numbers (see pioneering experiments by Kapitza & Kapitza 1949, and more recent ones by Liu, Jonathan & Gollub 1993) are not considered here. They are formed in laminar flows, and both viscosity and often surface tension play an important role (see, for example Prokopiou, Cheng & Chang 1991; Ruyer-Quil & Manneville 1998, and others) which is not the case for turbulent roll waves. The state of the art of the 'Kapitza waves' can be found, in particular, in a recent book by Charru (2011).

The first scientific observations of the turbulent roll waves are due to Cornish (1934) who observed this phenomenon in different channels and artificial conduits in Switzerland. The roll waves appearing initially have variable wave amplitudes and lengths, but then the phenomenon of coarsening happens where the waves of large amplitude overtake the waves of small amplitude producing larger waves. Under some

† Email address for correspondence: sergey.gavrilyuk@polytech.univ-mrs.fr

https://doi.org/10.1017/jfm.2012.96 Published online by Cambridge University Press

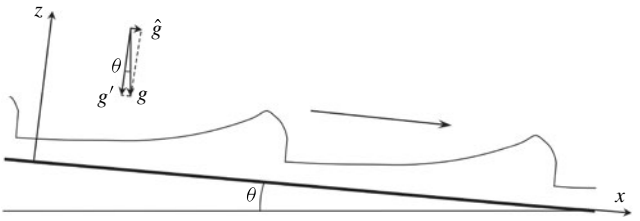


FIGURE 1. A typical profile of roll waves down an inclined plane of angle θ in Brock's experiments (1967).

circumstances, a system of periodic roll waves can be observed. Cornish studied, in particular, this phenomenon in the artificial conduit beside the funicular which connected Territet with Glion in Switzerland: 'within a few yards from the summit at Glion, the flickering flow of the very shallow current is transformed into an orderly procession of small, progressive waves with straight, frothing fronts, ranged squarely across channel'. He also noted that 'the space between the wave-crests steadily increased until a maximum of about 2 feet was attained. This was long before the end of the run, and thereafter the procession underwent no further change' (Cornish 1934). The stationary system of roll waves is not observed systematically: a long channel is needed. It is difficult to have channels long enough to attain the periodic structure of waves in laboratories. Spontaneous roll waves are, in general, non-periodic and non-permanent. However, Brock (1967, 1969, 1970) was able to obtain a periodic system of roll waves by applying a periodic perturbation at the inlet of the channel. Such a perturbation accelerated the roll waves formation. Roll waves are convective instabilities, i.e. any disturbance grows in the reference frame moving with the flow but decreases in the laboratory reference frame because the structures are carried downstream. As a consequence, roll waves are extremely sensitive to external noise near the flow inlet (see also Liu *et al.* 1993 for convective instabilities in film flows at smaller Reynolds numbers). Roll waves act therefore as noise amplifiers which can explain why periodic waves can be obtained by a periodic perturbation at the inlet of the channel.

Brock measured the stationary wave profiles in different conditions (different slopes and wall roughness). He noticed that the roll wave profiles always contain the following three essential parts: first, a sudden increasing of the depth since all waves break, i.e. acquire steeply sloping wave fronts; second, a continuous zone where the depth increases progressively; and third, a slowly decreasing zone until reaching a new hydraulic jump (see figure 1). The second part of the wave profile is neglected in the well-known mathematical model by Dressler (1949) where the maximal depth is attained immediately behind the shock. In particular, Brock (1967, 1969, 1970) noticed serious discrepancies between Dressler's model and experiments, except for low slopes. This is due to the fact that the second zone where the wave amplitude is increasing progressively, cannot be neglected.

A theoretical description of shear effects, i.e. vertically non-uniform velocity in the fluid flow, could be an important issue in roll waves modelling. These hydraulic jumps or bores are turbulent: a large-scale vortex flow forms immediately behind the shock, and dissipates progressively along the wave. Their structure was recently studied, in particular, in Misra *et al.* (2008) in the case of hydraulic jumps. The aim of this article

https://doi.org/10.1017/jfm.2012.96 Published online by Cambridge University Press

is to propose a theoretical model of shear flows of shallow water down an inclined plane.

The paper is organized as follows. In § 2, we derive a new model for the description of shear flows of shallow water. First, the conservative part of the model is established. Then, the dissipative terms are added in accordance with basic physical principles. The model is hyperbolic, so we study the Rankine–Hugoniot relations associated with the conservative formulation of the model. In § 3 we present stationary solutions of the new model describing roll waves. In § 4 we compare the solutions obtained to Brock's measurements. Mathematical details are given in appendices A, B and C.

2. Derivation of the model

2.1. *Motivation*

A traditional formulation of shallow water flows down an inclined plane is based on the Saint Venant equations. Let H be a characteristic fluid depth, and λ be a characteristic wavelength. The long-wave approximation supposes that the ratio $\varepsilon = H/\lambda$ is small. If, additionally, the horizontal velocity is uniform in the layer, one obtains the following system of Saint Venant equations (Whitham 1974):

$$\frac{\partial h}{\partial t} + \frac{\partial hu}{\partial x} = 0, \quad \frac{\partial hu}{\partial t} + \frac{\partial hu^2 + g'h^2/2}{\partial x} = \hat{g}h - C_f|u|u. \tag{2.1}$$

Here $h(x,t)$ is the water depth, $u(x,t)$ is the velocity in the x-direction, $g' = g\cos\theta$ and $\hat{g} = g\sin\theta$, where θ is the inclination angle (see figure 1). The driving force in the momentum equation is $\hat{g}h$, and the friction force is $-C_f|u|u$, C_f being the friction coefficient depending on the wall roughness as well as on the Reynolds number. The Saint Venant equations are hyperbolic. When shocks (hydraulic jumps) appear, the Rankine–Hugoniot relations arising from the conservative form (2.1) should be satisfied:

$$[h(u-D)] = 0, \quad \left[hu(u-D) + \frac{g'h^2}{2}\right] = 0. \tag{2.2}$$

Here D is the shock velocity, and $[X] = X_L - X_R$ is the jump of any variable X where X_L and X_R are its values at the left and at the right, respectively. Right (left)-facing shocks are shocks where $h_L > h_R$ ($h_L < h_R$). The energy equation can be obtained from (2.1):

$$\frac{\partial}{\partial t}\left(\frac{1}{2}hu^2 + \frac{1}{2}g'h^2\right) + \frac{\partial}{\partial x}\left(\frac{1}{2}hu^3 + g'h^2u\right) = (\hat{g}h - C_f|u|u)u. \tag{2.3}$$

However, the energy determined by (2.3) is not conserved through the jumps. It gives instead the inequality (Whitham 1974):

$$-D\left[\tfrac{1}{2}hu^2 + \tfrac{1}{2}g'h^2\right] + \left[\tfrac{1}{2}hu^3 + g'h^2u\right] < 0. \tag{2.4}$$

In particular, (2.4) implies that some energy is dissipated throughout the hydraulic jumps. This inequality plays the same role as the entropy inequality for the Euler equation of compressible fluids. Dressler (1949) obtained a periodic discontinuous solution to this system describing stationary roll waves and satisfying throughout the hydraulic jumps the 'entropy inequality' (2.4).

The fact that the energy is not conserved throughout the hydraulic jumps means that such a description is not completely satisfactory. Indeed, these hydraulic jumps are

https://doi.org/10.1017/jfm.2012.96 Published online by Cambridge University Press

always turbulent: the velocity is highly non-uniform in the z-direction (see Misra *et al.* 2008). And this non-uniformity was not taken into account in (2.1). Equations (2.1) are indeed an approximation of the following equations (Kranenburg 1992; Balmforth & Mandre 2004):

$$\frac{\partial h}{\partial t}+\frac{\partial hU}{\partial x}=0,\quad \frac{\partial hU}{\partial t}+\frac{\partial}{\partial x}\int_0^h u^2(x,z,t)\,\mathrm{d}z+g'h\frac{\partial h}{\partial x}=\hat{g}h-C_f|U|U, \tag{2.5}$$

where U is the horizontal velocity averaged over the fluid depth. Neglecting the shear effects inside the layer is equivalent to using system (2.1). An empirical approach to take the shear effects into account consists of introducing a parameter α such that

$$\alpha=\frac{\displaystyle\int_0^h u^2\,\mathrm{d}z}{hU^2}. \tag{2.6}$$

This parameter is usually assumed to be constant in the flow. However, as was noticed by Kranenburg (1992), this is certainly not the case, because 'in the bores a surface roller occurs, and the recirculating flow results in velocity profiles that are very non-uniform'. For turbulent flows this parameter is usually taken equal to 1, which is equivalent to neglecting the shear. However, even if $\alpha\neq 1$, it does not change the general behaviour of solutions (Kranenburg 1992). If $\alpha\neq 1$, (2.5) lose the property of Galilean invariance. Also, system (2.5) does not admit the energy conservation law with the total energy in the form

$$E=\tfrac{1}{2}hU^2+e_i(h) \tag{2.7}$$

where $e_i(h)$ is the potential energy (see appendix A for the proof).

Hydraulic jumps in Dressler's theory have a zero thickness while experimentally this thickness is finite. To improve the model (2.1), Needham & Merkin (1984) proposed introducing a turbulent viscosity into the Saint Venant equations:

$$\frac{\partial h}{\partial t}+\frac{\partial hu}{\partial x}=0,\quad \frac{\partial u}{\partial t}+u\frac{\partial u}{\partial x}+g'\frac{\partial h}{\partial x}=\hat{g}-C_f\frac{|u|u}{h}+\nu\frac{\partial^2 u}{\partial x^2}. \tag{2.8}$$

Here ν is the turbulent (eddy) viscosity. Adding the viscosity corresponds to the classical Prandtl hypothesis in modelling turbulent flows. In particular, Needham & Merkin (1984) constructed smooth roll wave solutions to this system.

One can rigorously derive the viscosity term from the Navier–Stokes equations only for laminar flows by imposing a parabolic profile of the horizontal velocity (Prokopiou *et al.* 1991; Gerbeau & Perthame 2001). However, such a derivation cannot be applied to turbulent flows. Indeed, a constant parabolic profile throughout the flow depth is unlikely, especially in the area behind the jump where large-scale eddies or 'rollers' are present.

A small turbulent viscosity does not significantly improve the results because the viscous roll waves are practically the same as those of Dressler. This is linked with the convergence of the viscous roll wave solutions toward the non-viscous Dressler's roll wave solutions when the viscosity goes to zero. As was pointed out by Yu & Kevorkian (1992), 'inclusion of a diffusive term multiplied by a small parameter will have a significant effect only in a thin layer centred at a bore, and will smooth the discontinuity'. A large turbulent viscosity gives wave shapes which are also very different from the experimental ones (see Needham & Merkin 1984, p. 275).

https://doi.org/10.1017/jfm.2012.96 Published online by Cambridge University Press

Finally, the viscous model always gives smooth profiles. It entirely removes the shock-like part of the stationary roll waves. However, this part was clearly observed by Brock (1970, p. 2567) who noted: 'The profile consists of a vertical front immediately upstream of h_{min}, followed by a portion where h increases rather gradually to h_{max} over a distance λ_S'. The vertical front of roll waves can be the location of specific physical phenomena such as air entraining.

The combination of the two parameters α and ν also does not provide a fit to experimental data. Therefore, a new theoretical model describing roll waves with strong shear effects is needed.

2.2. *Conservative part of the model*

2.2.1. *Shear flows of ideal fluids*

We derive here a general model of ideal shear flows of shallow water. The derivation partially follows Teshukov (2007). For simplicity, we consider the flow over the horizontal plane ($\theta = 0$), so the gravity vector is in the z-direction: $\boldsymbol{g} = (0, -g)^{\mathrm{T}}$. Let ε be a small parameter of long waves. Making a standard dimensionless analysis we arrive at the Euler equations in the following form:

$$\frac{\partial u}{\partial x} + \frac{\partial w}{\partial z} = 0, \quad \frac{\partial u}{\partial t} + \frac{\partial u^2}{\partial x} + \frac{\partial wu}{\partial z} + g\frac{\partial h}{\partial x} = O(\varepsilon^2). \tag{2.9}$$

Here u is the horizontal velocity, w is the vertical velocity. Introducing the mean horizontal velocity

$$U = \langle u \rangle = \frac{1}{h}\int_0^h u(t, x, z)\,\mathrm{d}z \tag{2.10}$$

and its fluctuation u' by $u = U + u'$, after integrating (2.9) over the fluid depth and using the boundary conditions

$$w = 0 \quad \text{at } z = 0, \quad \frac{\partial h}{\partial t} + u\frac{\partial h}{\partial x} = w \quad \text{at } z = h(x, t), \tag{2.11}$$

we obtain the following system of equations reminiscent of (2.5):

$$\frac{\partial h}{\partial t} + \frac{\partial hU}{\partial x} = 0, \quad \frac{\partial hU}{\partial t} + \frac{\partial hU^2 + gh^2/2 + h\langle u'^2\rangle}{\partial x} = O(\varepsilon^2). \tag{2.12}$$

Here

$$\langle u'^2\rangle = \frac{1}{h}\int_0^h u'^2\,\mathrm{d}z. \tag{2.13}$$

Multiplying the second equation of (2.9) by u we obtain

$$\frac{\partial u^2}{\partial t} + \frac{\partial u^3}{\partial x} + \frac{\partial wu^2}{\partial z} + 2ug\frac{\partial h}{\partial x} = O(\varepsilon^2). \tag{2.14}$$

Averaging (2.14) over the fluid depth we arrive at

$$\frac{\partial}{\partial t}(hU^2 + h\langle u'^2\rangle) + \frac{\partial}{\partial x}(hU^3 + 3hU\langle u'^2\rangle + h\langle u'^3\rangle) + U\frac{\partial gh^2}{\partial x} = O(\varepsilon^2). \tag{2.15}$$

An important question to ask would be whether the second- and third-order correlations are negligible with respect to the higher-order terms $O(\varepsilon^2)$ coming from the classical shallow-water approximation. We will estimate these terms for a special class of weakly sheared flows.

https://doi.org/10.1017/jfm.2012.96 Published online by Cambridge University Press

2.2.2. *Weakly sheared flows*

We say that the flow is *weakly sheared* if

$$\sqrt{\frac{H}{g}}\frac{\partial u}{\partial z} = O(\varepsilon^{\alpha}), \quad \alpha > 0. \tag{2.16}$$

Here H is a characteristic vertical scale. This property is time invariant in the case of long waves: if, initially, the flow is weakly sheared then for any time it will be weakly sheared. Indeed, in the long-wave approximation the dimensionless vorticity is

$$-\sqrt{\frac{H}{g}}\frac{\partial u}{\partial z} + O(\varepsilon^2). \tag{2.17}$$

Since in the two-dimensional case the vorticity is conserved along trajectories, we get

$$\frac{H}{g}\frac{\mathrm{D}}{\mathrm{D}t}\left(\frac{\partial u}{\partial z}\right) = O(\varepsilon^2) \tag{2.18}$$

where the material derivative is defined as

$$\frac{\mathrm{D}}{\mathrm{D}t} = \frac{\partial}{\partial t} + u\frac{\partial}{\partial x} + w\frac{\partial}{\partial z}. \tag{2.19}$$

It follows from (2.18) that for any time

$$\sqrt{\frac{H}{g}}\frac{\partial u}{\partial z} = O(\varepsilon^{\beta}), \quad \beta = \min(\alpha, 2), \tag{2.20}$$

if initially it satisfies (2.16). In particular this implies that

$$\frac{\langle u'^2\rangle}{gH} = O(\varepsilon^{2\beta}). \tag{2.21}$$

Indeed, for any z belonging to $(0, h)$ we have

$$\begin{aligned}
|u - U| &= \left|u - \frac{1}{h}\int_0^h u\,\mathrm{d}z\right| \\
&= \left|\int_0^z \frac{\partial u}{\partial z}\,\mathrm{d}z - \frac{1}{h}\int_0^h \left(\int_0^{z'} \frac{\partial u}{\partial z}\,\mathrm{d}z\right)\mathrm{d}z'\right| \\
&\leqslant \int_0^z \left|\frac{\partial u}{\partial z}\right|\mathrm{d}z + \frac{1}{h}\int_0^h\int_0^{z'}\left|\frac{\partial u}{\partial z}\right|\mathrm{d}z\,\mathrm{d}z' \\
&\leqslant \max_{0\leqslant z\leqslant h}\left|\frac{\partial u}{\partial z}\right|\left(\int_0^h \mathrm{d}z + \frac{1}{h}\int_0^h z'\,\mathrm{d}z'\right) \\
&= \frac{3h}{2}\max_{0\leqslant z\leqslant h}\left|\frac{\partial u}{\partial z}\right|.
\end{aligned} \tag{2.22}$$

Hence,

$$\frac{\langle u'^2\rangle}{gH} = \frac{1}{h}\int_0^h \frac{|u - U|^2}{gH}\,\mathrm{d}z = O(\varepsilon^{2\beta}). \tag{2.23}$$

https://doi.org/10.1017/jfm.2012.96 Published online by Cambridge University Press

Analogously,

$$\frac{\langle u'^3\rangle}{(gH)^{3/2}} = O(\varepsilon^{3\beta}). \tag{2.24}$$

Finally, if $\beta > 1$, $\langle u'^2\rangle$ can be neglected and, *a fortiori*, $\langle u'^3\rangle$. The system is then reduced to the classical shallow-water equations. If $\beta < 1$, the term $\langle u'^2\rangle$ cannot be neglected because it is now a lower-order term with respect to $O(\varepsilon^2)$. On the contrary, $\langle u'^3\rangle$ is now negligible with respect to $U\langle u'^2\rangle$, so that the total error will be $O(\max(\varepsilon^2, \varepsilon^{3\beta}))$. Finally, the governing equations in the case where the second-order correlations are important will be

$$\frac{\partial h}{\partial t} + \frac{\partial hU}{\partial x} = 0, \tag{2.25}$$

$$\frac{\partial hU}{\partial t} + \frac{\partial}{\partial x}\left(hU^2 + \frac{gh^2}{2} + h\langle u'^2\rangle\right) = 0, \tag{2.26}$$

$$\frac{\partial}{\partial t}\left(\frac{h}{2}\left(U^2 + gh + \langle u'^2\rangle\right)\right) + \frac{\partial}{\partial x}\left(hU\left(\frac{U^2}{2} + gh + \frac{3}{2}\langle u'^2\rangle\right)\right) = 0. \tag{2.27}$$

Here we have dropped higher-order terms on the right-hand side of the equations. The corresponding derivation in the three-dimensional case can be found in Teshukov (2007).

2.2.3. *Analogy with compressible fluids*

Equations (2.25)–(2.27) are reminiscent of the Euler equations of compressible fluids with the specific internal energy given by

$$e = \frac{gh}{2} + \frac{\langle u'^2\rangle}{2} \tag{2.28}$$

and the pressure:

$$p = \frac{gh^2}{2} + h\langle u'^2\rangle. \tag{2.29}$$

The corresponding 'Gibbs identity' can be written in the form

$$\mathrm{d}e + p\,\mathrm{d}\tau = \frac{1}{2\tau^2}\,\mathrm{d}\eta. \tag{2.30}$$

Here $\tau = 1/h$ is the analogue of a 'specific volume', and $\eta = \tau^2\langle u'^2\rangle$ having the dimension of the squared vorticity, is the analogue of the 'specific entropy'. Indeed, as a consequence of (2.25)–(2.27), the 'specific entropy' is conserved along trajectories:

$$\frac{\partial \eta}{\partial t} + U\frac{\partial \eta}{\partial x} = 0. \tag{2.31}$$

The equations are hyperbolic with the characteristic speeds $c_1 < c_2 < c_3$ where $c_1 = U - a$, $c_2 = U$ and $c_3 = U + a$. The sound speed a for the Euler equations of compressible fluids is defined as

$$a^2 = -\tau^2 \left.\frac{\partial p}{\partial \tau}\right|_{\eta=\text{const}}. \tag{2.32}$$

https://doi.org/10.1017/jfm.2012.96 Published online by Cambridge University Press

Since

$$p = \frac{g\tau^{-2}}{2} + \tau^{-3}\eta \tag{2.33}$$

we obtain

$$a = \sqrt{gh + 3\langle u'^2\rangle}. \tag{2.34}$$

2.3. *Dissipative part of the model*

In this section, (2.25)–(2.27) will be modified to the case of an inclined plane with friction effects.

2.3.1. *Turbulence study*

It is important to distinguish at least two scales of the velocity fluctuations due to shear effects. A small scale corresponds to the shear flow near the wall, while a large scale corresponds to the shear flow formed in the hydraulic jump. We decompose the turbulent energy as

$$\langle u'^2\rangle = \langle u'^2\rangle_s + \langle u'^2\rangle_\ell \tag{2.35}$$

where indexes s and ℓ correspond to the small-scale vorticity generated at the bottom and the large-scale vorticity generated in the shock. Writing each term in the form

$$\langle u'^2\rangle_s = \omega^2 h^2, \quad \langle u'^2\rangle_\ell = \Omega^2 h^2, \tag{2.36}$$

we associate this presentation with the decomposition of the total flow vorticity into a small-scale vorticity ω created near the wall, and a large-scale vorticity Ω created in the shock. The squared vorticities play the role of the different 'entropies'. In fluid mechanics the squared vorticities are usually called 'enstrophies'. For greater convenience, we will denote them by φ and Φ:

$$\varphi = \omega^2 = \frac{\langle u'^2\rangle_s}{h^2}, \quad \Phi = \Omega^2 = \frac{\langle u'^2\rangle_\ell}{h^2}. \tag{2.37}$$

We will suppose that the small-scale enstrophy φ defined by (2.37) is conserved:

$$\frac{\partial}{\partial t}(h\varphi) + \frac{\partial}{\partial x}(hU\varphi) = 0. \tag{2.38}$$

In particular, (2.38) implies that φ does not evolve in hydraulic jumps:

$$[\varphi] = 0. \tag{2.39}$$

On the contrary, the large-scale enstrophy Φ evolves: it appears just behind the jump where it attains its maximum, and then progressively disappears. The jump of Φ and its evolution is determined from (2.25)–(2.27). A two-scale decomposition such as (2.35)–(2.37) appears in other domains of physics also. For example, in plasma physics two types of entropy are present: the entropy of electrons and the entropy of ions. When shocks are studied, the classical conservation laws of mass, momentum and energy are not sufficient to close the system of Rankine–Hugoniot relations. Additional physical assumptions are needed. Such an assumption is, in particular, the conservation of the entropy of electrons through the shock (they are too small to be influenced by the shock); only the ion entropy jumps (Zel'dovich & Raizer 2001). Analogous closure problems related to multi-temperature and multi-entropy physics appear for shock wave propagation in compressible turbulent flows and multi-phase flows (Gavrilyuk & Saurel 2006, 2007).

https://doi.org/10.1017/jfm.2012.96 Published online by Cambridge University Press

2.3.2. *Friction force in the momentum equation*

Among friction forces which are present in the shear flow we have to distinguish the external forces due to the wall friction, and the internal forces acting during the interaction of the main fluid flow with a large-scale turbulent region appearing in the hydraulic jump (roller eddies). Both forces participate in the horizontal momentum balance. Experimental studies of hydraulic jumps (Misra *et al.* 2008) show that the large-scale turbulence is concentrated mainly in the upper part of the flow (breaker shear layer). The experimental results also indicate that there is a natural upward flow flux to this breaker shear layer from a nearly irrotational flow below. This upward momentum diffusion is associated with a natural drag force for the horizontal average momentum. We will describe this complex two-dimensional phenomenon by introducing the global friction force in the form $-C|U|U$ where

$$C=\frac{\left\langle u'^2\right\rangle_s}{\langle u'^2\rangle_s+\langle u'^2\rangle_\ell}C_f+\frac{\langle u'^2\rangle_\ell}{\langle u'^2\rangle_s+\langle u'^2\rangle_\ell}C_T=\frac{\varphi}{\varphi+\Phi}C_f+\frac{\Phi}{\varphi+\Phi}C_T. \tag{2.40}$$

Here C_T is a new friction coefficient associated with the interaction of the mean flow with large-scale eddies (rollers). *A priori*, it should be smaller than C_f. Equation (2.40) implies that $C_T<C<C_f$.

If $\varphi\gg\Phi$, i.e. the wall friction dominates over the internal friction, we obtain the classical friction coefficient C_f, while if $\varphi\ll\Phi$, i.e. the internal friction dominates over the wall friction, the friction coefficient is C_T. So, the momentum balance equation will be

$$\frac{\partial hU}{\partial t}+\frac{\partial}{\partial x}\left(hU^2+\frac{g'h^2}{2}+(\varphi+\Phi)h^3\right)=\hat{g}h-C|U|U, \tag{2.41}$$

where the friction coefficient C is determined by (2.40).

2.3.3. *The energy balance*

The dissipativeless energy equation (2.27) already contains all types of energies related to the fluid flow (micro- and macro-kinetic energy and potential energy). The wall friction force is the external force to the system. The work of this force is then $-C_f|U|U^2$. In the case of an inclined plane, (2.27) is transformed to

$$\begin{aligned}&\frac{\partial}{\partial t}\left(\frac{h}{2}(U^2+g'h+(\varphi+\Phi)h^2)\right)+\frac{\partial}{\partial x}\left(hU\left(\frac{U^2}{2}+g'h+\frac{3}{2}(\varphi+\Phi)h^2\right)\right)\\&\quad=\left(\hat{g}h-C_f|U|U\right)U.\end{aligned} \tag{2.42}$$

We have replaced in the energy equation (2.27) the gravity g by a reduced gravity $g'=g\cos\theta$, and have added the work of the driving force $\hat{g}h$ and the work of the external friction force $-C_f|U|U^2$. In particular, the momentum equation (2.41), the energy equation (2.42) and the mass conservation law imply the balance equation for the large-scale enstrophy Φ:

$$h^3\frac{\mathrm{D}\Phi}{\mathrm{D}t}=2(C-C_f)|U|U^2<0. \tag{2.43}$$

As $C<C_f$, the large-scale enstrophy decreases. It is generated in hydraulic jumps (as is the case of the entropy for the Euler equations of compressible fluids); however, it decreases in time (which is the opposite of the classical entropy behaviour).

https://doi.org/10.1017/jfm.2012.96 Published online by Cambridge University Press

2.4. *Final system of equations*

We finally obtain the following system of equations for the description of shear flows of shallow water down an inclined plane:

$$\frac{\partial h}{\partial t} + \frac{\partial hU}{\partial x} = 0, \tag{2.44}$$

$$\frac{\partial hU}{\partial t} + \frac{\partial}{\partial x}\left(hU^2 + \frac{g'h^2}{2} + (\varphi + \Phi)h^3\right) = \hat{g}h - C|U|U, \tag{2.45}$$

$$\frac{\partial}{\partial t}(hE) + \frac{\partial}{\partial x}\left(hU\left(E + \frac{p}{h}\right)\right) = \left(\hat{g}h - C_f|U|U\right)U, \tag{2.46}$$

$$\frac{\partial}{\partial t}(h\varphi) + \frac{\partial}{\partial x}(hU\varphi) = 0. \tag{2.47}$$

Here the total specific energy E, the internal specific energy e, the pressure p and the friction coefficient C are defined as

$$E = \tfrac{1}{2}U^2 + e, \quad e = \tfrac{1}{2}(g'h + (\varphi + \Phi)h^2), \tag{2.48}$$

$$p = \frac{g'h^2}{2} + (\varphi + \Phi)h^3, \tag{2.49}$$

$$C = \frac{\varphi}{\varphi + \Phi}C_f + \frac{\Phi}{\varphi + \Phi}C_T. \tag{2.50}$$

The characteristic speeds of (2.44)–(2.47) are

$$c_1 < c_2 = c_3 < c_4 \tag{2.51}$$

where

$$c_1 = U - a^*, \quad c_2 = c_3 = U, \quad c_4 = U + a^* \tag{2.52}$$

and a^* is the 'sound speed':

$$a^* = \sqrt{g'h + 3(\varphi + \Phi)h^2}. \tag{2.53}$$

2.4.1. *Stability of uniform flows*

As in the case of the classical Saint Venant equations, system (2.44)–(2.47) with closure relations (2.48)–(2.50) admits solutions describing uniform flows:

$$h = \text{const}, \quad \varphi = \text{const}, \quad \Phi = 0, \quad U = \sqrt{\hat{g}h/C_f}. \tag{2.54}$$

In appendix B we have established that the flow is stable if the following conditions are satisfied:

$$C_f > C_T \tag{2.55}$$

and

$$F^* < 2. \tag{2.56}$$

Here the generalized Froude number F^* is defined as

$$F^* = \frac{U}{a^*} \tag{2.57}$$

https://doi.org/10.1017/jfm.2012.96 Published online by Cambridge University Press

where a^* is defined by (2.53). The generalized Froude number F^* is related to the classical Froude number $F = U/\sqrt{g'h}$ by the formula

$$F = F^* \sqrt{1 + \frac{3(\varphi + \Phi)h}{g'}}. \tag{2.58}$$

In terms of the classical Froude number, the uniform flow loses its stability for $F > 2\sqrt{1 + (3(\varphi + \Phi)h)/g'} > 2$. Inequality (2.56) shows, in particular, consistency of the physical hypotheses which were necessary for establishing the governing equations.

2.5. *Rankine–Hugoniot relations*

For the shock propagating with velocity D, the Rankine–Hugoniot relations for system (2.44)–(2.47) are

$$[h(U - D)] = 0, \tag{2.59}$$

$$\left[h\,(U - D)^2 + \frac{g'h^2}{2} + (\varphi + \Phi)h^3\right] = 0, \tag{2.60}$$

$$\left[\tfrac{1}{2}\,(U - D)^2 + g'h + \tfrac{3}{2}(\varphi + \Phi)h^2\right] = 0, \tag{2.61}$$

$$[\varphi] = 0. \tag{2.62}$$

As usual, the jump of any variable X is denoted by $[X] = X_L - X_R$, where X_L and X_R are the values of X at the left and at the right of the shock. Denoting

$$m = h(U - D) \tag{2.63}$$

we obtain the following expressions for the Rayleigh line and the Hugoniot curve of centre R:

$$p - p_R + m^2(\tau - \tau_R) = 0, \quad \tau = h^{-1}, \tag{2.64}$$

$$e - e_R + \tfrac{1}{2}(p + p_R)(\tau - \tau_R) = 0. \tag{2.65}$$

The Hugoniot curve (2.65) and the curve (2.49) with $\Phi = 0$ are osculatory at R. Using (2.64)–(2.65) we can link the states at the left and right sides of the discontinuity:

$$p_L\left(\tau_L - \frac{\tau_R}{2}\right) + p_R\left(\frac{\tau_L}{2} - \tau_R\right) + \frac{g'}{4}\left(\frac{1}{\tau_L} - \frac{1}{\tau_R}\right) = 0. \tag{2.66}$$

Once the state R is given, one can determine the state L as the intersection of the Rayleigh line and the Hugoniot curve (see figure 2). Obviously, if R is the state before the jump, we always have

$$h_R < h_L < 2h_R. \tag{2.67}$$

Hence, the jump amplitude h_L/h_R does not exceed 2. On the contrary, the large-scale enstrophy Φ can considerably increase. The jump of Φ is defined by

$$\Phi_L - \Phi_R = \frac{\tau_R - \tau_L}{4}\frac{(\tau_R - \tau_L)^2}{\tau_R(\tau_L - \tau_R/2)}\left(g'\frac{\tau_L}{\tau_R} + \frac{2}{\tau_R^2}(\tau_R + \tau_L)(\varphi + \Phi_R)\right). \tag{2.68}$$

It follows from (2.68) that the sign of $\Phi_L - \Phi_R$ is the same as that of $\tau_R - \tau_L$. This sign is positive for right-facing waves. So, the large-scale enstrophy behaves like the 'entropy' for Euler equations of compressible fluids: it increases through the shocks. Also, $\Phi_L \to \infty$ if $\tau_L \to \tau_R/2$.

https://doi.org/10.1017/jfm.2012.96 Published online by Cambridge University Press

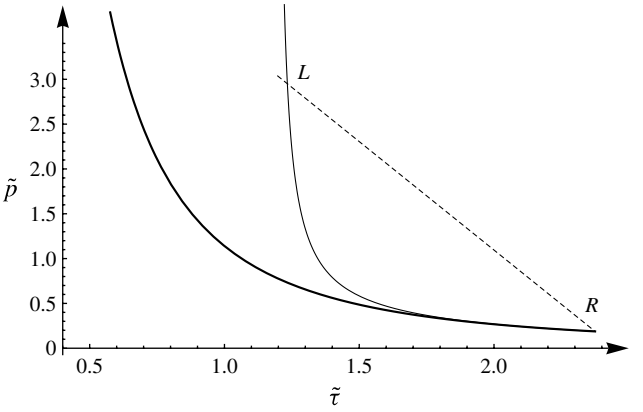


FIGURE 2. The state L behind the hydraulic jump is determined as the intersection of the Rayleigh line (dashed line), and the Hugoniot curve (thin curve). The Hugoniot curve and the curve $\Phi = 0$ (bold curve) are osculatory at R.

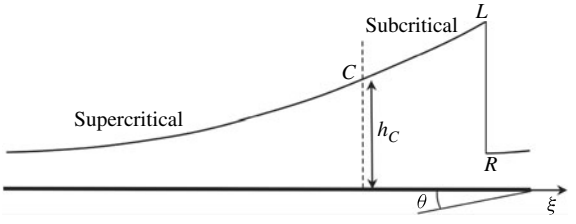


FIGURE 3. A typical wave profile of Dressler's solution is shown. The flow before the jump (state R) is supercritical, while behind the jump (state L) it is subcritical. There exists a critical point in the flow C where the wave velocity is characteristic. Then the depth is decreasing to attain the state R.

3. Roll wave solutions

3.1. *Comparison of Dressler's solution with Brock's experiments*

The first theoretical description of roll wave solutions to (2.1) was proposed by Dressler (1949). This solution is a periodic system of hydraulic jumps separated by smooth profiles. A typical Dressler's solution is shown in figure 3. The speed of the long gravity waves being $a = \sqrt{g'h}$, the flow is supercritical before the jump ($D > u_R + a_R$), while behind the jump it is subcritical ($D < u_L + a_L$). There exists a critical point C in the smooth part of the profile where $D = u_C + a_C$, $a_C = \sqrt{g'h_C}$ (see figure 3). Much work has been done on the stability of roll wave solutions both to system (2.1) and (2.8). In particular, Boudlal & Liapidevskii (2005) studied the modulation stability of roll wave solutions to (2.1), Noble (2006, 2007) studied the spectral stability of roll wave solutions to inviscid system (2.1), and the linear stability of roll waves to viscous system (2.8). The main qualitative result of that study is the stability of waves of large amplitude.

Brock (1970) noticed that there are serious discrepancies between Dressler's theory and experimental results, except for slopes $\sim 2\,\%$: 'the results from the theory for small slopes are found to be in considerable disagreement with the experimental results, except for smallest slopes'. According to Brock, the main disagreement is

https://doi.org/10.1017/jfm.2012.96 Published online by Cambridge University Press

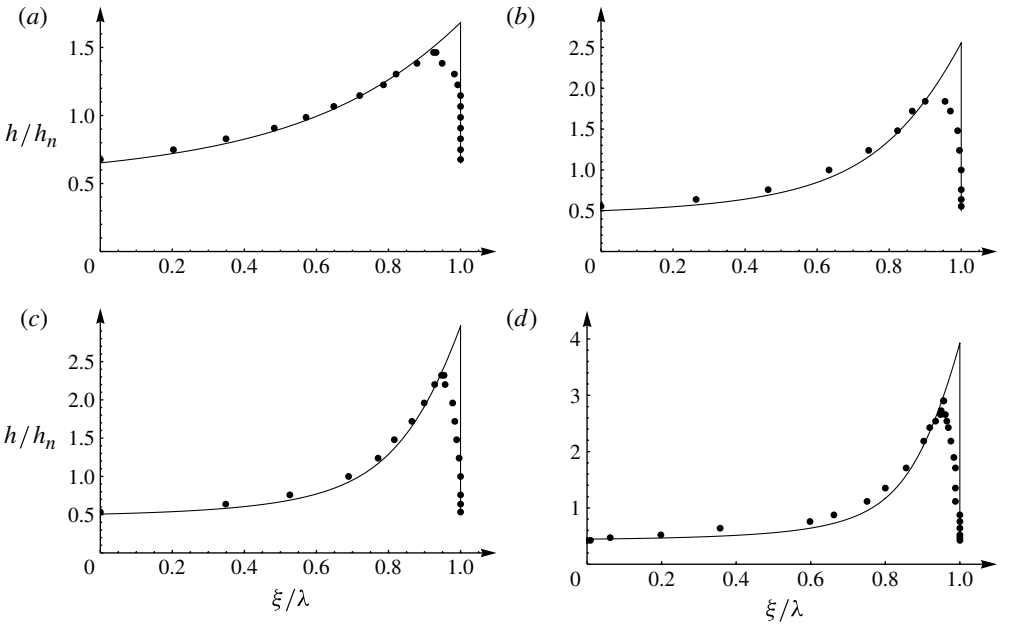


FIGURE 4. Comparison of Brock's experiments (dots) and Dressler's solutions (curves) for different slopes $S = \tan\theta$: (*a*) $S = 0.0502$, (*b*) $S = 0.0846$, (*c*) $S = 0.0846$, (*d*) $S = 0.1201$. In (*b*) and (*c*) the slopes were the same, however the wavelengths λ were different. A detailed description of Brock's experiments will be given in section 4. The experimental profiles h/h_n are presented as a function of ξ/λ where h is the fluid depth, h_n is the normal depth of a uniform inlet flow, λ is the stationary wavelength, and ξ is the horizontal coordinate in the reference frame moving with the wave.

that hydraulic jumps in Dressler's theory have a zero thickness while experimentally this thickness is finite. Also, the wave amplitude is largely overestimated in Dressler's theory (see figure 4 where we compared Dressler's solution with Brock's experiments). The introduction of a constant viscosity does not improve the situation. Small viscosities just smooth the wave profile and always overestimate the wave amplitude (see, for example Chang, Demekhin & Kalaidin 2000). A large turbulent viscosity changes drastically the solution profile: the part corresponding to the sharp jump disappears while it is always present in experiments.

3.2. *Equations of roll waves*

We are looking for stationary solutions in the reference frame moving with the waves. The solutions to our system depend only on $\xi = x - Dt$, where D is the wave velocity. Equations (2.44)–(2.47) imply

$$h(U - D) = m = \text{const} < 0, \tag{3.1}$$

$$\frac{\mathrm{d}}{\mathrm{d}\xi}\left(\frac{m^2}{h} + \frac{g'h^2}{2} + (\varphi + \Phi)h^3\right) = \hat{g}h - CU^2, \tag{3.2}$$

$$\frac{\mathrm{d}\varphi}{\mathrm{d}\xi} = 0, \tag{3.3}$$

$$\frac{\mathrm{d}\Phi}{\mathrm{d}\xi} = -2\Delta C\frac{\Phi}{\varphi + \Phi}\frac{U^3}{mh^2}, \quad \Delta C = C_f - C_T > 0. \tag{3.4}$$

https://doi.org/10.1017/jfm.2012.96 Published online by Cambridge University Press

Since the waves are faster than the mean fluid velocity, the constant m is negative. Developing the momentum equation we obtain

$$\left(g'h - \frac{m^2}{h^2} + 3(\varphi + \Phi)h^2\right)\frac{\mathrm{d}h}{\mathrm{d}\xi} + h^3\frac{\mathrm{d}\Phi}{\mathrm{d}\xi} = \hat{g}h - CU^2. \tag{3.5}$$

The governing equations after the jump are then

$$\frac{\mathrm{d}\Phi}{\mathrm{d}\xi} = -2\Delta C\frac{\Phi}{\varphi + \Phi}\frac{U^3}{mh^2} \tag{3.6}$$

$$\frac{\mathrm{d}h}{\mathrm{d}\xi} = \frac{\hat{g}h - CU^2 + 2\Delta C\dfrac{\Phi}{\varphi + \Phi}\dfrac{hU^3}{m}}{g'h + 3(\varphi + \Phi)h^2 - \dfrac{m^2}{h^2}}, \quad \Delta C = C_f - C_T > 0, \tag{3.7}$$

where the mean flow velocity is determined from the mass conservation law:

$$U = D + \frac{m}{h}. \tag{3.8}$$

Equations (3.6)–(3.7) are the basic equations for the analysis of roll wave solutions.

3.3. *Critical point*

The critical point C of (3.6)–(3.7) is a point where $\Phi_C = 0$ and $D = U_C + a_C^*$. We will use the index C for the flow parameters at the critical point. As in Dressler's model, we will construct a periodic solution such that the flow is supercritical before the jump ($D > U_R + a_R^*$) and subcritical after the jump ($D < U_L + a_L^*$). We will also show that the large-scale enstrophy exists only in a relatively narrow region behind the shock where there are turbulent eddies or rollers. In the remaining part of the wave, this large-scale enstrophy is very small. The constant m can be expressed in terms of critical parameters as

$$m = h_C(U_C - D) = -h_C a_C^*. \tag{3.9}$$

The denominator of (3.7) vanishes at the critical point. In order to have a finite slope at the critical point, the numerator of (3.7) must also vanish:

$$\hat{g}h_C(\varphi + \Phi_C) - (\varphi C_f + \Phi_C C_T)U_C^2 - 2\Delta C\Phi_C\frac{U_C^3}{a_C^*} = 0. \tag{3.10}$$

Since φ is constant everywhere in the flow, we do not use index C for this variable. The point $(h_C, \Phi_C = 0)$ is a linearly unstable fixed point of system (3.6)–(3.7) (see appendix C). At the point $(h_C, \Phi_C = 0)$ the condition (3.10) takes the form

$$U_C = \sqrt{\frac{\hat{g}h_C}{C_f}}. \tag{3.11}$$

We have obtained the same condition as in Dressler's model.

3.4. *Dimensionless variables*

Let us introduce now dimensionless variables defined as

$$\tilde{h} = \frac{h}{h_C}, \quad \tilde{\xi} = \frac{\xi}{h_C}, \quad \tilde{\varphi} = \frac{\varphi h_C}{g'}, \quad \tilde{\Phi} = \frac{\Phi h_C}{g'}, \quad \tilde{p} = \frac{2p}{g'h_C^2}. \tag{3.12}$$

https://doi.org/10.1017/jfm.2012.96 Published online by Cambridge University Press

Since $D = U_C + a_C^*$ and $U = D + m/h$, we also obtain

$$U = a_C \left(1 + F_C^* - \frac{1}{\tilde{h}}\right), \quad F_C^* = U_C/a_C^*. \tag{3.13}$$

This allows us to put (3.6)–(3.7) into the following dimensionless form:

$$\frac{\mathrm{d}\tilde{h}}{\mathrm{d}\tilde{\xi}} = \frac{\tilde{h}^3 \tan\theta - \dfrac{1+3\tilde{\varphi}}{\tilde{\varphi}+\tilde{\Phi}}\left(\tilde{h}\left(1+F_C^*\right)-1\right)^2\left(\tilde{\varphi}C_f + \tilde{\Phi}C_T + 2\Delta C\tilde{\Phi}\left(\tilde{h}\left(1+F_C^*\right)-1\right)\right)}{(\tilde{h}-1)\left(\tilde{h}^2+\tilde{h}+1+3\tilde{\varphi}\left(\tilde{h}+1\right)\left(\tilde{h}^2+1\right)\right)+3\tilde{\Phi}\tilde{h}^4}, \tag{3.14}$$

$$\frac{\mathrm{d}\tilde{\Phi}}{\mathrm{d}\xi} = 2\Delta C(1+3\tilde{\varphi})\frac{\tilde{\Phi}}{\tilde{\varphi}+\tilde{\Phi}}\frac{\left(1+F_C^*-\dfrac{1}{\tilde{h}}\right)^3}{\tilde{h}^2}. \tag{3.15}$$

Condition (3.11) can be also written as

$$\tan\theta = C_f F_C^{*2}(1+3\tilde{\varphi}). \tag{3.16}$$

At the critical point we have $\tilde{\Phi}_C = 0$. It follows from (3.15) that all derivatives of $\tilde{\Phi}$ with respect to ξ vanish at C. Hence, calculating the derivative of $\tilde{h}$ with respect to $\tilde{\xi}$ we can just put $\tilde{\Phi} = 0$ to obtain the following equation for $\tilde{h}$ in the vicinity of the critical point:

$$\frac{\mathrm{d}\tilde{h}}{\mathrm{d}\tilde{\xi}} = \frac{\tilde{h}^3\tan\theta - C_f\left(1+3\tilde{\varphi}\right)\left(\tilde{h}\left(1+F_C^*\right)-1\right)^2}{\left(\tilde{h}-1\right)\left(\tilde{h}^2+\tilde{h}+1+3\tilde{\varphi}\left(\tilde{h}+1\right)\left(\tilde{h}^2+1\right)\right)}. \tag{3.17}$$

Using condition (3.16) we get

$$\frac{\mathrm{d}\tilde{h}}{\mathrm{d}\tilde{\xi}} = \frac{\tan\theta}{F_C^{*2}}\frac{\tilde{h}^3F_C^{*2} - \left(\tilde{h}\left(1+F_C^*\right)-1\right)^2}{\left(\tilde{h}-1\right)\left(\tilde{h}^2+\tilde{h}+1+3\tilde{\varphi}\left(\tilde{h}+1\right)\left(\tilde{h}^2+1\right)\right)}. \tag{3.18}$$

Factorization of the numerator and the denominator by $(\tilde{h}-1)$ (since $\tilde{h}=1$ is a common root of the two functions) implies finally the equation

$$\frac{\mathrm{d}\tilde{h}}{\mathrm{d}\tilde{\xi}} = \tan\theta\frac{\tilde{h}^2 - \dfrac{1+2F_C^*}{F_C^{*2}}\tilde{h} + \dfrac{1}{F_C^{*2}}}{\tilde{h}^2+\tilde{h}+1+3\tilde{\varphi}\left(\tilde{h}+1\right)\left(\tilde{h}^2+1\right)}. \tag{3.19}$$

Hence, the slope estimated at the critical point is

$$\left(\frac{\mathrm{d}\tilde{h}}{\mathrm{d}\tilde{\xi}}\right)_C = \frac{\tan\theta}{F_C^*}\frac{\left(F_C^*-2\right)}{3+12\tilde{\varphi}}. \tag{3.20}$$

Since this slope must be positive, the condition of existence of roll waves is in the form

$$F_C^* > 2. \tag{3.21}$$

This condition is the same as in Dressler's solution (Dressler 1949). However, the generalized Froude number now replaces the classical Froude number.

https://doi.org/10.1017/jfm.2012.96 Published online by Cambridge University Press

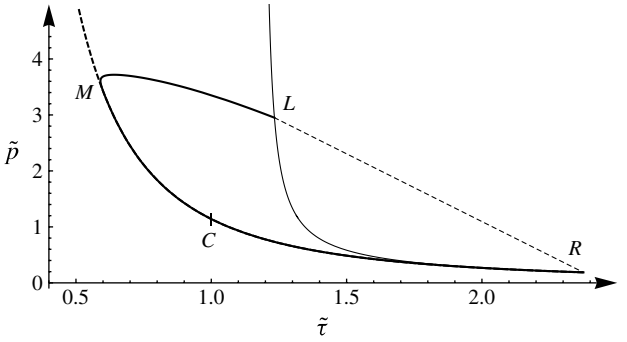


FIGURE 5. The solution curve (in bold) is shown in $(\tilde{\tau}, \tilde{p})$-plane. The Rayleigh line (dashed line) connects states L and R. The Hugoniot curve is shown by a thin line. The curve $\tilde{\Phi} = 0$ (bold dashed line) practically coincides with the solution curve beginning at point M where the maximum depth is attained: the value of $\tilde{\Phi}$ at M is almost negligible with respect to that at L. At the point C we have $\tilde{\Phi} = 0$.

3.5. *Construction of roll wave solutions*

The construction of a stationary periodic solution of (2.44)–(2.47) can easily be understood in the $(\tilde{\tau}, \tilde{p})$-plane (see figure 5), where $\tilde{\tau} = 1/\tilde{h}$, $\tilde{p} = \tilde{h}^2 + 2(\tilde{\varphi} + \tilde{\Phi})\tilde{h}^3$. Indeed, at the state R we have $\tilde{\Phi}_R = 0$, and, *a priori*, $\tilde{\varphi}_R \neq 0$. Jumping from the state R along the Rayleigh line (2.64) to the state L on the Hugoniot curve (2.65), we satisfy the Rankine–Hugoniot relations (2.59)–(2.62). The dimensionless large-scale enstrophy $\tilde{\Phi}_L$ increases through the jump. Then, we solve numerically the system of ordinary differential equations (3.14)–(3.15) with initial data $(\tilde{h}_L, \tilde{\Phi}_L)$. The solution approaches very quickly the state C where $\tilde{h}_C = 1$, $\tilde{\Phi}_C = 0$. Indeed, we have proved in appendix C that the critical point is linearly unstable (for increasing values of ξ), with one positive eigenvalue and one zero eigenvalue. Thus, it is linearly stable for decreasing values of ξ. When ξ decreases, one can numerically check that the critical point C is indeed nonlinearly asymptotically stable, and it is attained for a finite value of ξ. Then the solution follows the curve $\tilde{\Phi} = 0$ until the point R. Along the curve $C \to R$ the solution satisfies (3.14) where we have to put $\tilde{\Phi} = 0$:

$$\frac{\mathrm{d}\tilde{h}}{\mathrm{d}\tilde{\xi}} = \frac{\tan\theta \left(\tilde{h} - \tilde{h}_+\right)\left(\tilde{h} - \tilde{h}_-\right)}{\tilde{h}^2 + \tilde{h} + 1 + 3\tilde{\varphi}\left(\tilde{h} + 1\right)\left(\tilde{h}^2 + 1\right)}, \tag{3.22}$$

where

$$\tilde{h}_+ = \frac{1}{2F_C^*}\left(2 + \frac{1}{F_C^*} + \sqrt{\left(2 + \frac{1}{F_C^*}\right)^2 - 4}\right), \tag{3.23}$$

$$\tilde{h}_- = \frac{1}{2F_C^{*2}}\left(2 + \frac{1}{F_C^{*2}} - \sqrt{\left(2 + \frac{1}{F_C^*}\right)^2 - 4}\right). \tag{3.24}$$

https://doi.org/10.1017/jfm.2012.96 Published online by Cambridge University Press

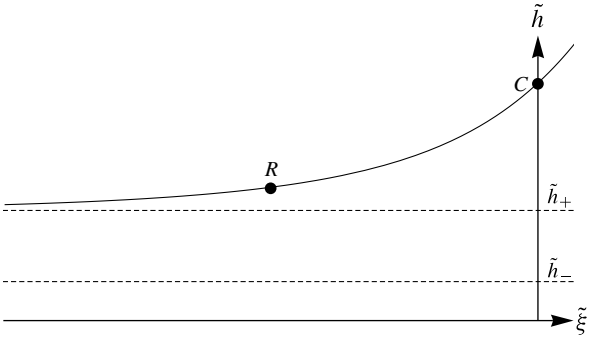


FIGURE 6. The roll wave solution branch. The solution tends to $\tilde{h}_+$ as $\tilde{\xi} \to -\infty$, and to infinity as $\tilde{\xi} \to +\infty$.

One can integrate (3.22) and obtain the equation of the free surface in implicit form:

$$\tilde{\xi} \tan\theta = \left(\tilde{h} - \tilde{h}_C\right)\left(1 + 3\tilde{\varphi}\left(\frac{3+\tilde{h}}{2} + \tilde{h}_+ + \tilde{h}_-\right)\right) + A_+ \ln\frac{\tilde{h} - \tilde{h}_+}{\tilde{h}_C - \tilde{h}_+} - A_- \ln\frac{\tilde{h} - \tilde{h}_-}{\tilde{h}_C - \tilde{h}_-} \tag{3.25}$$

with

$$\tilde{h}_C = 1, \tag{3.26}$$

$$A_+ = \frac{1 + \tilde{h}_+ + \tilde{h}_+^2 + 3\tilde{\varphi}\left(1 + \tilde{h}_+ + \tilde{h}_+^2 + \tilde{h}_+^3\right)}{\tilde{h}_+ - \tilde{h}_-}, \tag{3.27}$$

$$A_- = \frac{1 + \tilde{h}_- + \tilde{h}_-^2 + 3\tilde{\varphi}\left(1 + \tilde{h}_- + \tilde{h}_-^2 + \tilde{h}_-^3\right)}{\tilde{h}_+ - \tilde{h}_-}. \tag{3.28}$$

The solution (3.25) is determined up to an additive constant. It coincides with Dressler's solution (Dressler 1949) if we put $\tilde{\varphi} = 0$. The roll wave solution corresponds to the branch $\tilde{h} > \tilde{h}_+$ (obviously, we have $\tilde{h}_+ > \tilde{h}_-$). Moreover, $\tilde{h}(\xi) \to \tilde{h}_+$ as $\tilde{\xi} \to -\infty$, and $\tilde{h} \to +\infty$ as $\tilde{\xi} \to +\infty$ (see figure 6). Consequently, along this branch $\tilde{h}_R$ necessarily satisfies

$$\tilde{h}_R > \tilde{h}_+. \tag{3.29}$$

To construct the roll wave solution, one chooses a point R on the curve $\tilde{\Phi} = 0$ satisfying (3.29) and such that $\tilde{h}_R < 1$. The point L is found by the Rankine–Hugoniot relations. The profiles of $\tilde{h}$ and $\tilde{\Phi}$ are then calculated by solving numerically (3.14)–(3.15). A typical wave profile is shown in figure 7. In figure 8, we show $\tilde{\Phi}$ and $\tilde{\varphi}$ as functions of ξ normalized by the wavelength in two cases corresponding to Brock's (1967) experiments. These experiments will be described in § 4. Whereas $\tilde{\varphi}$ is constant in the flow, $\tilde{\Phi}$ suddenly increases through the shock and decreases rather gradually after the shock. Its value becomes negligible around the point M, i.e. at the maximum fluid depth. At the critical point C and, beyond, to R, the large-scale enstrophy $\tilde{\Phi}$ is identically zero.

https://doi.org/10.1017/jfm.2012.96 Published online by Cambridge University Press

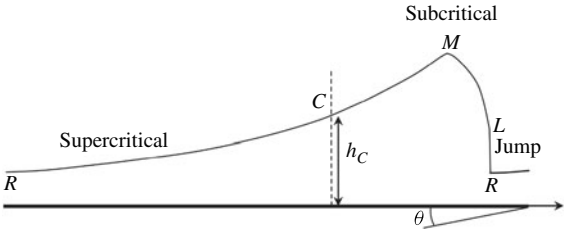


FIGURE 7. A typical wave profile for the new model. The flow before the jump (state R) is supercritical, while behind the jump (state L) it is subcritical. There exists the critical point C in the flow where the wave velocity is characteristic. After the jump $R \to L$ the wave depth increases to attain its maximal value at M. The fluid flow is always subcritical at M. Then the depth is decreasing to attain the state R. The solution curve from C to R is close to Dressler's solution because the value of $\tilde{\varphi}$ is small.

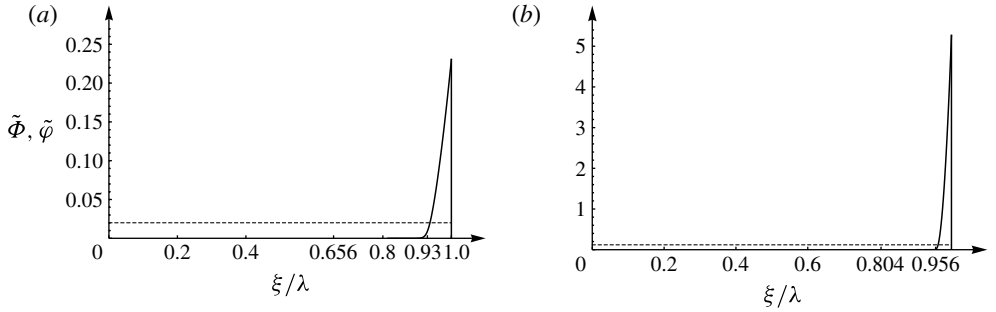


FIGURE 8. Variation of the large-scale enstrophy, $\tilde{\Phi}$ (continuous line), and of the small-scale enstrophy, $\tilde{\varphi}$ (dashed line) as a function of ξ/λ where λ is the wavelength. At $\xi/\lambda = 1$, $\tilde{\Phi}$ suddenly increases through the shock and then gradually decreases. (a) Case 1 of Brock's experiments (see table 2 below) corresponding to the smallest slope. $\xi/\lambda = 0.93$ at the point M (maximum depth) and $\xi/\lambda = 0.656$ at the critical point. (b) Case 9 of Brock's experiments (see table 2) corresponding to the largest slope. $\xi/\lambda = 0.956$ at the point M (of maximum depth) and $\xi/\lambda = 0.804$ at the critical point.

4. Comparison with Brock's experimental results

4.1. *Parameters of the uniform flow*

The roll wave solutions to the model (2.44)–(2.47) will now be compared to the very pertinent experimental results obtained by Brock (1967). All the numerical parameters measured in inches and feet, are transformed into IS units. Brock used a rectangular channel 36.6 m long with slopes of 0.0502 and 0.0846, and a smaller channel 24.4 m long with a slope of 0.1201. We define the slope by $\tan\theta$ instead of $\sin\theta$ used by Brock. The values of $\sin\theta$ were 0.05011, 0.08429 and 0.1192, respectively (Brock 1967, 1969, 1970). The width of the channel was 11.75 cm. The measurements were made for the long smooth bottom channel with two slopes, and for the shorter channel with a smooth and a rough bottom. The rough one was obtained by covering the bottom with sand grains with an average diameter of 0.6 mm. The biggest particles were approximately 1 mm diameter. As the channel length was not long enough to obtain natural stationary roll waves, periodic perturbations were introduced at the inlet to obtain a stationary roll wave train. The experimental profiles h/h_n were presented as a function of ξ/λ where h_n is the normal depth of a uniform inlet flow with the velocity U_n (so, $h_n U_n$ is the flow discharge), and λ is the stationary wavelength.

https://doi.org/10.1017/jfm.2012.96 Published online by Cambridge University Press

To compare our theoretical solution with Brock's experimental results, we have to express h_n in terms of the critical depth h_C. Let $q(\xi) = h(\xi)U(\xi)$ be the local flow discharge per unit width, and $\langle q \rangle$ be the average discharge per unit width:

$$\langle q \rangle = \frac{1}{\lambda}\int_0^\lambda q\,\mathrm{d}\xi = \frac{1}{\lambda}\int_0^\lambda hU\,\mathrm{d}\xi = \langle hU \rangle. \tag{4.1}$$

On the other hand,

$$\langle q \rangle = h_n U_n. \tag{4.2}$$

For uniform flows, $U_n = \sqrt{\hat{g}h_n/C_f}$. Mass conservation implies $hU = hD + m$, i.e. $hU = a_C(h(1 + F_C^*) - h_C)$. Taking the average over the period λ we obtain

$$h_n^{3/2} F_C \sqrt{g'} = a_C(\langle h \rangle (1 + F_C^*) - h_C). \tag{4.3}$$

Here

$$\langle h \rangle = \frac{1}{\lambda}\int_0^\lambda h\,\mathrm{d}\xi. \tag{4.4}$$

For the dimensionless normal depth $\tilde{h}_n = h_n/h_C$, we obtain the following relation:

$$\tilde{h}_n^{3/2} F_C = \sqrt{1 + 3\tilde{\varphi}}(\langle \tilde{h} \rangle (1 + F_C^*) - 1). \tag{4.5}$$

Since $F_C = F_C{}^* \sqrt{1 + 3\tilde{\varphi}}$, we have

$$\tilde{h}_n = \left(\frac{\langle \tilde{h} \rangle (1 + F_C^*) - 1}{F_C^*} \right)^{2/3}. \tag{4.6}$$

Once $\tilde{h}$ is calculated, $\tilde{h}_n$ can be found, and then $\tilde{h}/\tilde{h}_n$. Obviously, $h/h_n = \tilde{h}/\tilde{h}_n$ and $\xi/\lambda = \tilde{\xi}/\tilde{\lambda}$, where $\tilde{\lambda} = \lambda/h_C$.

For a given slope and a wall roughness, the friction coefficient C_f is fixed. For the channel used by Brock, h_n was between 2.5 mm and 1 cm, and the channel width b was 11.75 cm, and hence the ratio h/b was between 0.021 and 0.085. For a given Froude number $F = U_n/\sqrt{g'h_n}$, the friction coefficient used by Brock was $\hat{C}_f$:

$$\hat{C}_f \frac{b + 2h_n}{b} = \frac{\hat{g}h_n}{U_n^2} = \frac{\tan\theta}{F^2}. \tag{4.7}$$

The function

$$r = \frac{bh_n}{b + 2h_n} \tag{4.8}$$

is called the hydraulic radius. The difference between $\hat{C}_f$ and that used for very wide channels

$$C_f = \frac{\hat{g}h_n}{U_n^2} = \frac{\tan\theta}{F^2} \tag{4.9}$$

is not important. As we will see below, the shock wave thickness is mainly determined not by C_f, but by the difference between C_f and C_T. We recall that the internal drag coefficient C_T is related to the presence of a strong shear flow behind the jump.

https://doi.org/10.1017/jfm.2012.96 Published online by Cambridge University Press

4.2. *Determination of the model parameters*

For each experimental run, the slope $\tan\theta$, the nature of the bottom surface (smooth or rough), the discharge per unit width q and the period T (linked to the wavelength λ by $T = \lambda/D$) are well determined. Then the Froude number and the Reynolds number of the corresponding uniform flow are also well determined. Specifically, the depth of the uniform flow can be deduced from

$$h_n^{3/2} = q\sqrt{\frac{C_f}{\hat{g}}}. \tag{4.10}$$

The velocity of the uniform flow can be expressed by $U_n = \sqrt{\hat{g}h_n/C_f}$, the Froude number by $F = U_n/\sqrt{g'h_n}$ and the Reynolds number by $Re = 4rU_n/\nu$ where r and ν are respectively the hydraulic radius and the kinematic viscosity. The Reynolds number is $4q/\nu$ for a very wide channel. Consequently, for each experiment, $\tan\theta$, C_f and the period T are experimentally determined parameters. The only adjustable parameters are therefore $\tilde{\varphi}$ and C_T. Brock (1967) used the following dimensionless period:

$$T' = T\sqrt{\frac{g}{h_n}}\sin\theta. \tag{4.11}$$

Within the framework of Dressler's model, this expression can also be written as

$$T' = \frac{\tilde{\lambda}}{(1+F_C)\sqrt{\tilde{h}_n}}\tan\theta\sqrt{\cos\theta}. \tag{4.12}$$

In our model, the expression for the period is

$$T' = \frac{\tilde{\lambda}}{(1+F_C^*)\sqrt{\tilde{h}_n\,(1+3\tilde{\varphi})}}\tan\theta\sqrt{\cos\theta}. \tag{4.13}$$

However, it is not easy to impose T' and then to deduce the value of $\tilde{h}_R$. The procedure we used was the inverse: for a given value of $\tilde{h}_R$ we searched for the corresponding value of T'. If the latter did not match the value measured by Brock, we changed the value of $\tilde{h}_R$ and we reiterated the procedure until the difference was negligible. Experimental parameters in Brock's experiments are shown in table 1. The period T' depends essentially on the ratio $\tilde{h}_R/\tilde{h}_+$ which is always greater than one (see condition (3.29)). The period increases as the ratio decreases, and it goes to infinity if the ratio goes to one. It is thus possible to adjust the period in two different ways: by the choice of $\tilde{h}_R$ or $\tilde{\varphi}$. Indeed, because of the condition (3.16), for given $\tan\theta$ and C_f the value of F_C^* depends only on $\tilde{\varphi}$. Now, $\tilde{h}_+$ depends only on F_C^* (see (3.23)). Consequently, increasing $\tilde{\varphi}$ for a constant value of $\tilde{h}_R$ is equivalent to decreasing F_C^* and thus increasing $\tilde{h}_+$, and therefore the wavelength $\tilde{\lambda}$.

The coefficient C_T determines the position of the maximum depth M, i.e. the shock thickness. In fact, the shock thickness depends on ΔC but, as C_f is fixed for a given slope and bottom roughness, only the coefficient C_T can vary when the period varies. The variable ΔC determines how fast the large-scale enstrophy generated by the shock disappears thereafter in the flow, i.e. how fast the system converges to the curve $\tilde{\Phi} = 0$ (see figure 5), that is toward the solution (3.25). As the system practically reaches this curve approximately at the point M, ΔC determines the distance between L and M,

https://doi.org/10.1017/jfm.2012.96 Published online by Cambridge University Press

	Cases 1, 2	Cases 3–6	Cases 7–9	Cases 10, 11
$\sin\theta$	0.05011	0.08429	0.1192	0.1192
Discharge ($m^3\ s^{-1}$)	9.72×10^{-4}	6.52×10^{-4}	8.02×10^{-4}	4.86×10^{-4}
h_n (mm)	7.98	5.28	5.33	5.05
U_n ($m\ s^{-1}$)	1.04	1.05	1.28	0.832
F	3.71	4.63	5.60	3.74
Re	3.11×10^4	2.24×10^4	2.60×10^4	1.63×10^4
$\hat{C}_f$	0.0032	0.0036	0.0035	0.0078

TABLE 1. Values of parameters for a smooth (Cases 1–9) and a rough (Cases 10–11) bottom in Brock's (1967) experiments. The different cases of each column differ by the wavelength (see table 2).

which is exactly the shock thickness. The coefficient C_T must be adjusted in each case to correctly determine the position of M.

We imposed that the coefficient $\tilde{\varphi}$ depends only on the slope and on the nature (smooth or rough) of the bottom surface. Its dependence on the wave amplitude and the wavelength is supposed to be negligible. The various cases corresponding to the same slope and smooth bottom surface, which differ only in the period, can reasonably be reproduced with the same $\tilde{\varphi}$ coefficient.

However, if $\tilde{\varphi}$ is determined to optimize the adjustment for short periods, the value of h_{max}/h_n is systematically slightly underestimated for long periods. Conversely, if the adjustment is optimized for long periods, h_{max}/h_n is slightly overestimated for short ones. Finally, the adjustments were optimized on short periods because the variation of depth and of the local Reynolds number are smaller for short periods. This fits better the hypothesis of a constant friction coefficient C_f along the flow. In reality, this coefficient decreases if the Reynolds number increases, that is if the depth increases. Different experimental formulae of the dependence of C_f on the Reynolds number can be found, for example, in Thual (2010). The Darcy–Weisbach relation was found by Brock (1967) to fit his experimental data for a smooth bottom with an average deviation of only 2.2 %:

$$\frac{1}{\sqrt{f}} = 2.03 \log\left(Re\sqrt{f}\right) - 1.30 \tag{4.14}$$

where $f = 8C_f$.

For the model of Dressler, which already overestimates the maximum depth, the variation of C_f along the flow as a function of the local Reynolds number can only worsen the results. On the contrary, for our model, this variation would probably improve the results.

4.3. *Comparison with Brock's experiments and discussion*

Figures 9–11 show, for a smooth bottom surface, a comparison of the theoretical profiles obtained with the model (2.44)–(2.47) and the experimental results of Brock (1967, 1969, 1970). Since the period of roll waves was imposed by a periodic perturbation at the flow inlet where the roll waves were formed, Brock was able to obtain roll waves of various periods for the same slope. The numerical values of the model parameters are shown in table 2. Figure 9 shows the results for the slope equal to 0.0502, figure 10 corresponds to the slope equal to 0.0846, and figure 11

https://doi.org/10.1017/jfm.2012.96 Published online by Cambridge University Press

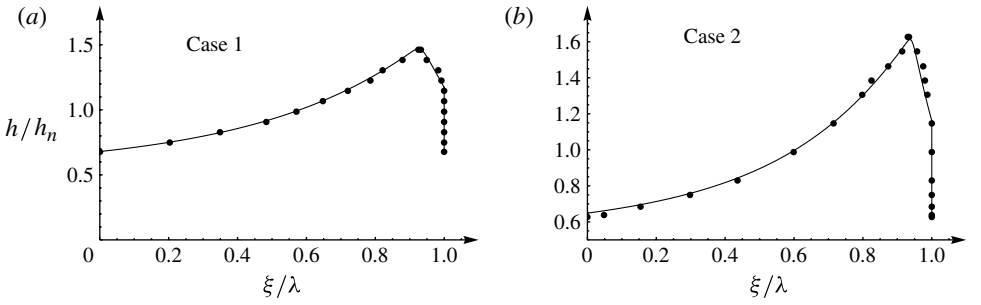


FIGURE 9. Comparison of the theoretical solution to the model (2.44)–(2.47) (line) and Brock's experimental results (dots) for $\tan\theta = 0.0502$. The flow parameters are given in table 2. The dimensionless wavelength $\tilde{\lambda}$ is equal to (*a*) 150.3 (Case 1) and (*b*) 192.0 (Case 2). Excellent agreement has been obtained.

corresponds to the slope equal to 0.1201. Experimental values are taken from table 7 of Brock's (1967) thesis. The agreement between the results of our model and the experimental results is very good. The first part of the profile representing a very steep depth increase (a jump for which we used the Rankine–Hugoniot relations) is reproduced with great accuracy in all the cases. The thickness of the shock, neglected in Dressler's model, is also correctly found in our model. It is easy to see that the water depth also increases in a continuous part after the jump. These parts of the profile are the main improvement predicted by our model. The decreasing part of the profile (after the critical point) also agrees with experimental data, and it is close to Dressler's profile.

Figure 12 shows how the bottom enstrophy $\tilde{\varphi}$ varies with the slope. When the latter increases, shearing increases and this explains why $\tilde{\varphi}$ also increases. The drag coefficient C_T decreases when the period increases, and therefore when the ratio h_{max}/h_{min} increases. It is possible to calculate in each case the local Reynolds number at the maximum depth. We will denote it Re_M. The internal drag force exists only in the part of the flow where $\tilde{\Phi}$ is important, i.e. between L and M. At this location, the local Reynolds number is larger than the Reynolds number of the inlet uniform flow. We defined the local Reynolds number at point M as $4h_M U_M/\nu$. This number increases with the wave period. One can see that C_T decreases almost linearly with Re_M (see figure 13).

The agreement between the results of our model and Brock's measurements is less satisfactory for the rough bottom than for the smooth one. These results are shown in figure 14. However, one can notice that the diameter d of sand grains (0.6 mm in average) used to make a rough bottom, is not negligible compared to the water depth. The value of the inundation ratio defined by Lawrence (1997) as h/d is between 5.3 and 14.3 if only the average grain diameter is taken into account. When the biggest grain diameter reaches 1 mm, the inundation ratio can even be smaller. Values of inundation ratio between 1 and 10 correspond to a marginal inundation regime (Lawrence 1997). For this regime, the friction coefficient quickly decreases when the inundation ratio increases. Further, the roughness elements affect the entire vertical flow field: eddies created by obstacles near the bottom affect the flow up to the free surface. Therefore, the validity of the shallow-water approximation for the case of a rough bottom is questionable.

https://doi.org/10.1017/jfm.2012.96 Published online by Cambridge University Press

https://doi.org/10.1017/jfm.2012.96 Published online by Cambridge University Press

	Case 1	Case 2	Case 3	Case 4	Case 5	Case 6	Case 7	Case 8	Case 9	Case 10	Case 11
$\tan\theta$	0.0502		0.0846				0.1201			0.1201	
C_f	0.0036		0.0039				0.0038			0.0085	
$\tilde{\varphi}$	0.02		0.07				0.12			0.185	
F_C^*	3.63		4.23				4.82			3.01	
$\tilde{h}_R$	0.630	0.579	0.576	0.462	0.421	0.412	0.456	0.384	0.350	0.748	0.648
C_T	0.00325	0.0031	0.0035	0.0029	0.0025	0.0023	0.0028	0.0024	0.0018	0.007	0.006
$\tilde{\lambda}$	150.3	192.0	106.8	179.8	242.6	265.7	119.4	178.7	246.2	80.2	146.7
$\tilde{h}_n$	0.927	0.893	0.928	0.834	0.763	0.740	0.874	0.785	0.700	0.955	0.884
$\tilde{T}'$	1.64	2.14	1.63	2.89	4.07	4.53	2.25	3.55	5.19	1.98	3.73

TABLE 2. Values of parameters for a smooth (Cases 1–9) and a rough (Cases 10–11) bottom used for comparison with Brock's experiments.

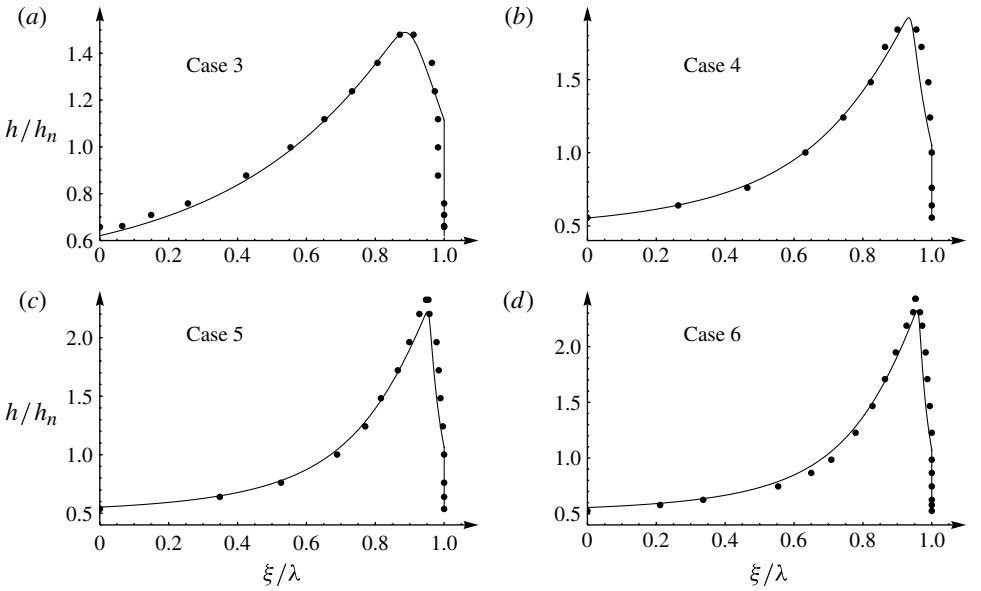


FIGURE 10. Comparison of the theoretical solution to the model (2.44)–(2.47) (line) and Brock's experimental results (dots) for $\tan\theta = 0.0846$. The flow parameters are given in table 2. The dimensionless wavelength $\tilde{\lambda}$ is equal to (*a*) 106.8 (Case 3), (*b*) 179.8 (Case 4), (*c*) 242.6 (Case 5), and (*d*) 265.7 (Case 6). A very good agreement has been obtained. The wave amplitude is slightly underestimated for large periods (Cases 5, 6), but the error is relatively small.

5. Conclusion

The model (2.44)–(2.47) describes shear flows of shallow water. The model is hyperbolic and reminiscent of the Euler equations of compressible fluids, but with two 'entropies'. These 'entropies' are indeed the flow enstrophies, i.e. the squared vorticities corresponding to two different flow scales. One of the enstrophies φ is associated with the small-scale turbulence generated near the bottom. It is conserved along the flow even in the presence of hydraulic jumps. The second enstrophy Φ is associated with the presence of large-scale roller eddies in the hydraulic jumps. Like the classical entropy, it increases in shocks. The stationary model contains two parameters. One is the above-mentioned small-scale enstrophy φ. It depends on the wall roughness, and the plane inclination. It increases if the plane slope increases. The second parameter C_T is associated with the internal drag force due to the presence of the roller vortex in the hydraulic jump. The number of empirical parameters in the model is also two as in the modified Saint Venant model with both profile correction coefficient α and the turbulent viscosity ν. However, though α and ν do not change the qualitative behaviour of the Dressler solution, our model fits the experimental results very well by accounting for both the shock thickness and the wave amplitude.

The stability properties of roll waves should still be studied. Even in the context of the Saint Venant equations, this question is not yet completely solved (see Barker *et al.* 2010). Indeed, constant states with Froude number larger than two are unstable, therefore the roll waves of very large length should also be unstable. And hence, stable roll waves, if they exist, must be of intermediate amplitude. The numerical study in

https://doi.org/10.1017/jfm.2012.96 Published online by Cambridge University Press

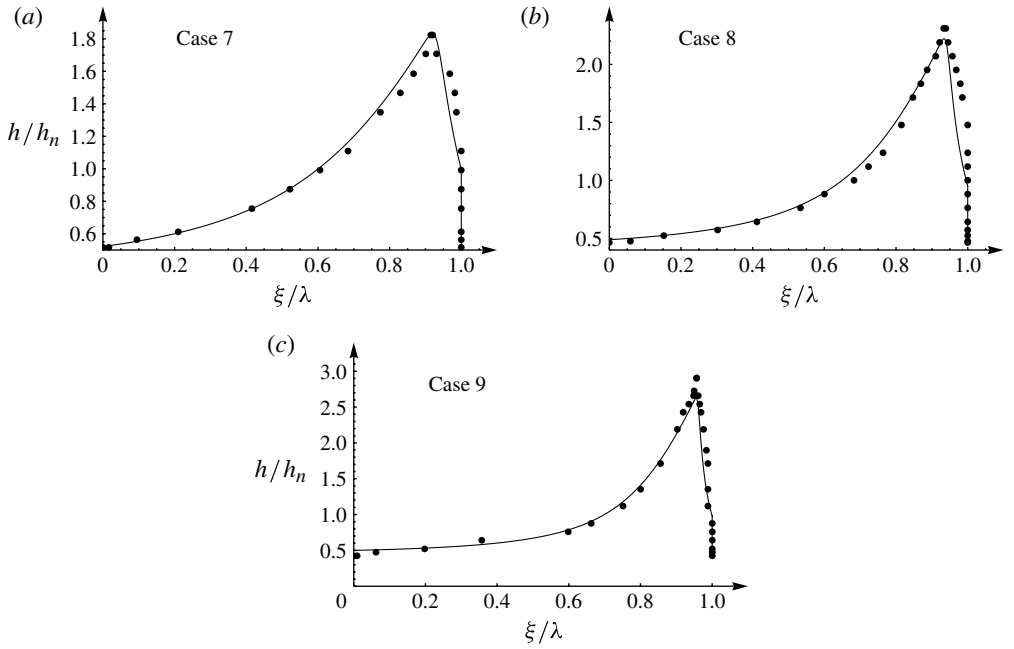


FIGURE 11. Comparison of the theoretical solution to the model (2.44)–(2.47) (line) and Brock's experimental results (dots) for $\tan\theta = 0.1201$. The flow parameters are given in table 2. The dimensionless wavelength $\tilde{\lambda}$ is equal to (*a*) 119.4 (Case 7), (*b*) 178.7 (Case 8) and (*c*) 246.2 (Case 9). A very good agreement has been obtained. The maximum wave amplitude is slightly underestimated for large periods (Cases 8, 9), but the error is relatively small.

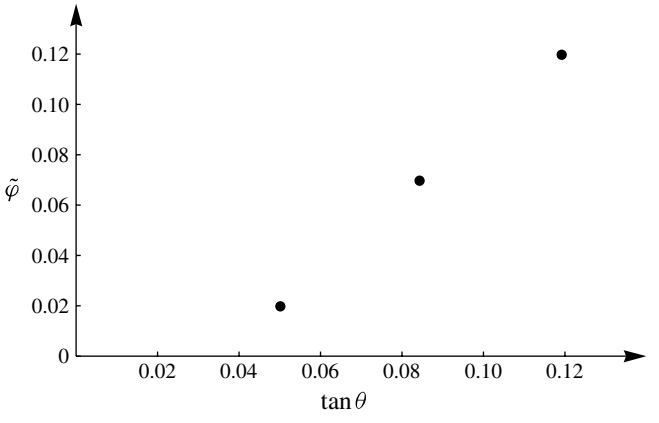


FIGURE 12. The small-scale enstrophy $\tilde{\varphi}$ characterizing shearing near the bottom increases with the slope.

Barker *et al.* (2010) shows that it is the case. We hope to confirm those results for the new model.

Another important issue will be the study of hydraulic jumps. There are several empirical correlations estimating the length of the roller of the hydraulic jump as a function of the upstream Froude number (see, for example Hager, Bremen & Kawagoshi 1990). Recently, we calculated the roller length and found a good

https://doi.org/10.1017/jfm.2012.96 Published online by Cambridge University Press

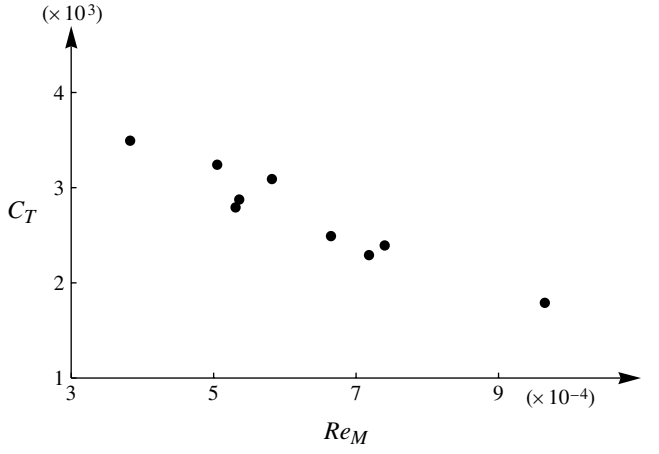


FIGURE 13. C_T decreases almost linearly as a function of the Reynolds number Re_M calculated at the point M. We only plotted the values of C_T for a smooth bottom as the case of a rough bottom is entirely different (the wall friction follows a different law).

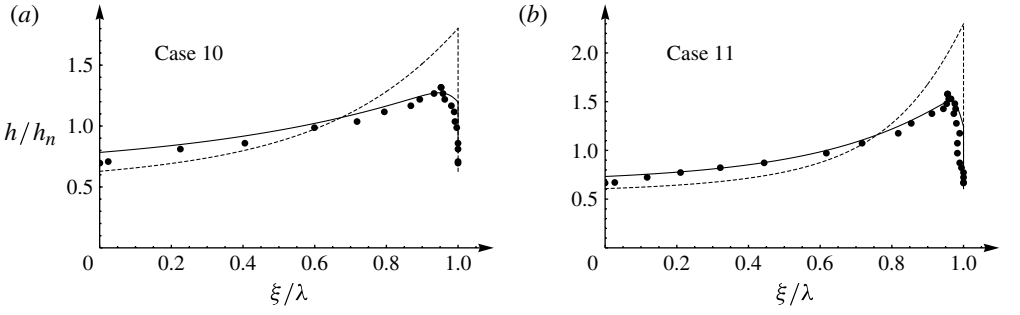


FIGURE 14. Comparison of the theoretical solution to the model (2.44)–(2.47) (solid line), Brock's experimental results (dots) and Dressler's solution (dashed line) for $\tan\theta = 0.1201$ and a rough bottom. The flow parameters are given in table 2. The dimensionless wavelength $\tilde{\lambda}$ is equal to (*a*) 80.2 (Case 10) and (*b*)146.7 (Case 11). The agreement between our theory and the Brock experiments is still good.

agreement with the proposed correlations. A detailed analysis of that study will be presented in a forthcoming paper.

Acknowledgements

We would like to thank the anonymous referees for providing us with constructive comments and suggestions.

Appendix A. Balance of energy

Consider (2.5) in variables $(h, q = hU)$:

$$\frac{\partial h}{\partial t} + \frac{\partial q}{\partial x} = 0, \quad \frac{\partial q}{\partial t} + \frac{\partial}{\partial x}\left(\alpha\frac{q^2}{h} + \frac{g'h^2}{2}\right) = \hat{g}h - C_f\frac{q^2}{h^2}. \tag{A 1}$$

https://doi.org/10.1017/jfm.2012.96 Published online by Cambridge University Press

We are looking for all conservation laws compatible with that system in the form

$$\frac{\partial e(h,q)}{\partial t}+\frac{\partial f(h,q)}{\partial x}=F(h,q) \tag{A 2}$$

with unknown functions $e(h,q)$, $f(h,q)$ and $F(h,q)$. We have

$$\frac{\partial e}{\partial t}=-\frac{\partial e}{\partial h}\frac{\partial q}{\partial x}-\frac{\partial e}{\partial q}\left(\frac{\partial}{\partial x}\left(\alpha\frac{q^2}{h}+\frac{g'h^2}{2}\right)-\hat{g}h+C_f\frac{q^2}{h^2}\right). \tag{A 3}$$

Also

$$\frac{\partial f}{\partial x}=\frac{\partial f}{\partial h}\frac{\partial h}{\partial x}+\frac{\partial f}{\partial q}\frac{\partial q}{\partial x}. \tag{A 4}$$

We finally obtain

$$-\frac{\partial e}{\partial h}\frac{\partial q}{\partial x}-\frac{\partial e}{\partial q}\frac{\partial}{\partial x}\left(\left(\alpha\frac{q^2}{h}+\frac{g'h^2}{2}\right)-\hat{g}h+C_f\frac{q^2}{h^2}\right)+\frac{\partial f}{\partial h}\frac{\partial h}{\partial x}+\frac{\partial f}{\partial q}\frac{\partial q}{\partial x}=F, \tag{A 5}$$

or

$$\frac{\partial h}{\partial x}\left(\alpha\frac{q^2}{h^2}\frac{\partial e}{\partial q}-g'h\frac{\partial e}{\partial q}+\frac{\partial f}{\partial h}\right)+\frac{\partial q}{\partial x}\left(-\frac{\partial e}{\partial h}-2\alpha\frac{q}{h}\frac{\partial e}{\partial q}+\frac{\partial f}{\partial q}\right)-\frac{\partial e}{\partial q}\left(-\hat{g}h+C_f\frac{q^2}{h^2}\right)=F. \tag{A 6}$$

This implies

$$\left.\begin{aligned}\frac{\partial f}{\partial h}&=\left(g'h-\alpha\frac{q^2}{h^2}\right)\frac{\partial e}{\partial q},\\ \frac{\partial f}{\partial q}&=\frac{\partial e}{\partial h}+2\alpha\frac{q}{h}\frac{\partial e}{\partial q},\\ \frac{\partial e}{\partial q}&\left(\hat{g}h-C_f\frac{q^2}{h^2}\right)=F.\end{aligned}\right\} \tag{A 7}$$

Differentiating the first equation of (A 7) with respect to q, and the second equation with respect to h, we obtain a partial differential equation for e:

$$\frac{\partial^2 e}{\partial h^2}+2\alpha\frac{q}{h}\frac{\partial^2 e}{\partial q\partial h}+\left(\alpha\frac{q^2}{h^2}-g'h\right)\frac{\partial^2 e}{\partial q^2}=0. \tag{A 8}$$

If the energy conservation law exists in a usual form

$$e=\frac{q^2}{2h}+e_i(h) \tag{A 9}$$

where $e_i(h)$ is an unknown function, we must have

$$\frac{q^2}{h^3}(1-\alpha)+\frac{\mathrm{d}^2 e_i}{\mathrm{d}h^2}-g'=0. \tag{A 10}$$

Since this compatibility condition should be valid for any q and h, we have

$$\frac{\mathrm{d}^2 e_i}{\mathrm{d}h^2}-g'=0,\quad \alpha=1. \tag{A 11}$$

https://doi.org/10.1017/jfm.2012.96 Published online by Cambridge University Press

Hence, up to an additive constant,

$$e = \frac{1}{2}hU^2 + \frac{g'h^2}{2} \tag{A 12}$$

and, necessarily, $\alpha = 1$.

Appendix B. Linear stability of uniform flows

Consider a uniform flow $h = h_0$, $U = U_0 = \sqrt{\hat{g}h_0/C_f}$, $\Phi = 0$, $\varphi = \varphi_0$. This implies $C = C_0 = C_f$. Let h', U', Φ' be perturbations of these quantities. Since φ is conserved along the trajectories, we do not need to consider perturbations of this variable. Let us also remark that

$$C' = -\frac{\Phi'}{\varphi_0}\Delta C, \quad \Delta C = C_f - C_T. \tag{B 1}$$

Introducing the material derivative

$$\frac{\partial}{\partial t} + U_0\frac{\partial}{\partial x} = \frac{\mathrm{D}_0}{\mathrm{D}t} \tag{B 2}$$

we obtain the following linearized system of equations arising from the mass conservation law:

$$\frac{\mathrm{D}_0 h'}{\mathrm{D}t} + h_0\frac{\partial U'}{\partial x} = 0, \tag{B 3}$$

the momentum conservation law

$$\frac{\mathrm{D}_0 U'}{\mathrm{D}t} + g'\frac{\partial h'}{\partial x} + 3\varphi_0 h_0\frac{\partial h'}{\partial x} + h_0^2\frac{\partial \Phi'}{\partial x} + \hat{g}\left(2\frac{U'}{U_0} - \frac{h'}{h_0} - \frac{\Delta C}{\varphi_0 C_f}\Phi'\right) = 0, \tag{B 4}$$

and the energy conservation law (which is equivalent to the evolution equation for Φ)

$$\frac{\mathrm{D}_0 \Phi'}{\mathrm{D}t} = -2\frac{U_0^3\Delta C}{h_0^3\varphi_0}\Phi'. \tag{B 5}$$

Taking the material derivative of (B 4) and using (B 3) and (B 5), we find the equation

$$\left(\frac{\partial}{\partial t} + c_+\frac{\partial}{\partial x}\right)\left(\frac{\partial}{\partial t} + c_-\frac{\partial}{\partial x}\right)U' + \frac{2\hat{g}}{U_0}\left(\frac{\partial}{\partial t} + c_0\frac{\partial}{\partial x}\right)U'$$
$$+ \frac{2U_0^3\Delta C}{h_0\varphi_0}\left(\frac{U_0^2\Delta C}{\varphi_0 h_0^3}\Phi' - \frac{\partial \Phi'}{\partial x}\right) = 0. \tag{B 6}$$

Here

$$\left.\begin{aligned} c_+ &= U_0 + a_0, \\ c_- &= U_0 - a_0, \\ c_0 &= \tfrac{3}{2}U_0, \\ a_0 &= \sqrt{g'h_0 + 3\varphi_0 h_0^2}. \end{aligned}\right\} \tag{B 7}$$

The velocities c_+ and c_- correspond to the characteristic velocities of the nonlinear system, while c_0 is the velocity of kinematic waves. If $\Delta C = 0$, (B 6) is reduced to

https://doi.org/10.1017/jfm.2012.96 Published online by Cambridge University Press

the classical equation in the linear stability theory for the Saint Venant equations (2.1). The expression

$$\frac{U_0^2\Delta C}{\varphi_0 h_0^3}\Phi' - \frac{\partial \Phi'}{\partial x} \tag{B 8}$$

can also be written as

$$\frac{1}{h_0^2}\left(\frac{\hat{g}\Delta C}{\varphi_0 C_f}\Phi' - h_0^2\frac{\partial \Phi'}{\partial x}\right). \tag{B 9}$$

Equation (B 4) implies

$$\frac{1}{h_0^2}\left(\frac{\hat{g}\Delta C}{\varphi_0 C_f}\Phi' - h_0^2\frac{\partial \Phi'}{\partial x}\right) = \frac{1}{h_0^2}\left(\frac{D_0 U'}{Dt} + (g' + 3\varphi_0 h_0)\frac{\partial h'}{\partial x} + \hat{g}\left(\frac{2U'}{U_0} - \frac{h'}{h_0}\right)\right). \tag{B 10}$$

Hence

$$\left(\frac{\partial}{\partial t} + c_+\frac{\partial}{\partial x}\right)\left(\frac{\partial}{\partial t} + c_-\frac{\partial}{\partial x}\right)U' + \frac{2\hat{g}}{U_0}\left(\frac{\partial}{\partial t} + c_0\frac{\partial}{\partial x}\right)U'$$
$$+ \frac{2U_0^3\Delta C}{h_0^3\varphi_0}\left(\frac{\mathrm{D}_0 U'}{\mathrm{D}t} + (g' + 3\varphi_0 h_0)\frac{\partial h'}{\partial x} + \hat{g}\left(\frac{2U'}{U_0} - \frac{h'}{h_0}\right)\right) = 0. \tag{B 11}$$

Taking once more the material derivative of (B 11) we obtain finally the equation for the velocity perturbation in the form

$$\left(\frac{\partial}{\partial t} + U_0\frac{\partial}{\partial x} + \frac{2U_0^3\Delta C}{h_0^3\omega^2}\right)$$
$$\times\left(\left(\frac{\partial}{\partial t} + c_+\frac{\partial}{\partial x}\right)\left(\frac{\partial}{\partial t} + c_-\frac{\partial}{\partial x}\right)U' + \frac{2\hat{g}}{U_0}\left(\frac{\partial}{\partial t} + c_0\frac{\partial}{\partial x}\right)U'\right) = 0. \tag{B 12}$$

We are looking for the solution of this equation in the form

$$U' = A\mathrm{e}^{\mathrm{i}k(x-ct)} \tag{B 13}$$

with k real and $c = c_r + \mathrm{i}c_i$. The stability condition is then $c_i < 0$. Substituting (B 13) into (B 12) we have

$$\left(-\mathrm{i}c + \mathrm{i}U_0 + \frac{2U_0^3\Delta C}{kh_0^3\varphi_0}\right)\left((-\mathrm{i}c + \mathrm{i}c_+)(-\mathrm{i}c + \mathrm{i}c_-) + \frac{2\hat{g}}{U_0 k}(-\mathrm{i}c + \mathrm{i}c_0)\right) = 0. \tag{B 14}$$

This equation is satisfied if one of the following equations is satisfied:

$$(-\mathrm{i}c + \mathrm{i}c_+)(-\mathrm{i}c + \mathrm{i}c_-) + \frac{2\hat{g}}{U_0 k}(-\mathrm{i}c + \mathrm{i}c_0) = 0, \tag{B 15}$$

$$-\mathrm{i}c + \mathrm{i}U_0 + \frac{2U_0^3\Delta C}{kh_0^3\varphi_0} = 0. \tag{B 16}$$

Following Whitham (1974), we can conclude that (B 15) has complex roots c with $c_i < 0$ if $c_- < c_0 < c_+$, i.e.

$$U_0 < 2\sqrt{g'h_0 + 3\varphi_0 h_0^2}. \tag{B 17}$$

https://doi.org/10.1017/jfm.2012.96 Published online by Cambridge University Press

Introducing the generalized Froude number F^* by

$$F^* = \frac{U}{a^*} = \frac{U}{\sqrt{g'h + 3(\varphi + \Phi)h^2}} \tag{B 18}$$

we can rewrite (B 17) in the form

$$F^* < 2. \tag{B 19}$$

This condition is similar to the stability of uniform flows for (2.1) (Jeffreys 1925; Whitham 1974) expressed in terms of the classical Froude number. Equation (B 16) implies

$$c_i = -\frac{2U_0^3 \Delta C}{kh_0^3 \varphi_0}. \tag{B 20}$$

The stability condition $c_i < 0$ is equivalent to $\Delta C > 0$. Finally, the uniform flow is stable if and only if

$$F^* < 2, \quad C_f > C_T. \tag{B 21}$$

Appendix C. Linear stability of the critical point

Equations (3.14)–(3.15) can be written in the form

$$\frac{\mathrm{d}\tilde{h}}{\mathrm{d}\tilde{\xi}} = \frac{N(\tilde{h}, \tilde{\Phi})}{D(\tilde{h}, \tilde{\Phi})}, \tag{C 1}$$

$$\frac{\mathrm{d}\tilde{\Phi}}{\mathrm{d}\tilde{\xi}} = G(\tilde{h}, \tilde{\Phi}). \tag{C 2}$$

The functions N and D are the numerator and the denominator of the corresponding rational function in (3.14). They vanish simultaneously at the critical point where $\tilde{h} = 1$, $\tilde{\Phi} = 0$. Instead of the variable ξ we introduce a new variable s such that

$$\frac{\mathrm{d}\tilde{\xi}}{\mathrm{d}s} = D(\tilde{h}, \tilde{\Phi}). \tag{C 3}$$

The governing equations are

$$\frac{\mathrm{d}\tilde{h}}{\mathrm{d}s} = N(\tilde{h}, \tilde{\Phi}), \quad \frac{\mathrm{d}\tilde{\Phi}}{\mathrm{d}s} = D(\tilde{h}, \tilde{\Phi})G(\tilde{h}, \tilde{\Phi}). \tag{C 4}$$

The point $(\tilde{h}, \tilde{\Phi}) = (1, 0)$ is a fixed point of (C 4). Linearizing in the vicinity of the fixed point

$$\tilde{h} = 1 + h', \tag{C 5}$$

$$\tilde{\Phi} = \Phi', \tag{C 6}$$

and calculating the derivatives

$$\frac{\partial N}{\partial \tilde{h}}(1, 0) = C_f F_C^*(F_C^* - 2)(1 + 3\tilde{\varphi}), \tag{C 7}$$

$$\frac{\partial N}{\partial \tilde{\Phi}}(1, 0) = -\Delta C {F_C^*}^2(2F_C^* - 1)\frac{1 + 3\tilde{\varphi}}{\tilde{\varphi}}, \tag{C 8}$$

https://doi.org/10.1017/jfm.2012.96 Published online by Cambridge University Press

$$\frac{\partial D\,G}{\partial \tilde{h}}(1,0)=0, \tag{C 9}$$

$$\frac{\partial D\,G}{\partial \Phi}(1,0)=0, \tag{C 10}$$

we obtain the following linear system of equations:

$$\frac{\mathrm{d}}{\mathrm{d}s}\begin{pmatrix} h' \\ \Phi' \end{pmatrix} = \begin{pmatrix} C_f F_C^*(F_C^*-2)(1+3\tilde{\varphi}) & -\Delta C {F_C^*}^2(2F_C^*-1)\dfrac{1+3\tilde{\varphi}}{\tilde{\varphi}} \\ 0 & 0 \end{pmatrix}\begin{pmatrix} h' \\ \Phi' \end{pmatrix}. \tag{C 11}$$

The eigenvalues of the corresponding matrix are

$$\lambda = 0 \tag{C 12}$$

and

$$\lambda = C_f F_C^*(F_C^*-2)(1+3\tilde{\varphi}). \tag{C 13}$$

For $\tilde{\xi}$ increasing with s (i.e. for $\tilde{h}>1$), the fixed point is unstable if

$$F_C^* > 2. \tag{C 14}$$

REFERENCES

BALMFORTH, N. J. & MANDRE, S. 2004 Dynamics of roll waves. *J. Fluid Mech.* **514**, 1–33.

BARKER, B., JOHNSON, M. A., NOBLE, P., RODRIGUES, L. M. & ZUMBRUN, K. 2010 Whitham averaged equations and modulational instability of periodic traveling waves of a hyperbolic–parabolic balance laws. arXiv:1008.4729v2 [math.AP] 3 Sept 2010.

BOUDLAL, A. & LIAPIDEVSKII, V. YU. 2005 Stability of regular roll waves. *Comput. Technol.* **10** (2), 3–14.

BROCK, R. R. 1967 Development of roll waves in open channels. PhD thesis, California Institute of Technology, Pasadena, California.

BROCK, R. R. 1969 Development of roll – wave trains in open channels. *J. Hydraul. Div. ASCE* **95**, 1401–1427.

BROCK, R. R. 1970 Periodic permanent roll waves. *J. Hydraul. Div. ASCE* **96**, 2565–2580.

CHANG, H.-C., DEMEKHIN, E. A. & KALAIDIN, E. 2000 Coherent structures, self-similarity, and universal roll wave coarsening dynamics. *Phys. Fluids* **12**, 2268–2278.

CHARRU, F. 2011 *Hydrodynamic Instabilities*. Cambridge University Press.

CORNISH, V. 1934 *Ocean Waves and Kindred Geophysical Phenomena*. Cambridge University Press.

DRESSLER, R. F. 1949 Mathematical solution of the problem of roll-waves in inclined open channels. *Commun. Pure Appl. Maths* **2**, 149–194.

GAVRILYUK, S. L. & SAUREL, R. 2006 Estimation of the turbulent energy production across a shock wave. *J. Fluid Mech.* **549**, 131–139.

GAVRILYUK, S. L. & SAUREL, R. 2007 Rankine–Hugoniot relations for shocks in heterogeneous mixtures. *J. Fluid Mech.* **575**, 495–507.

GERBEAU, J.-F. & PERTHAME, B. 2001 Derivation of viscous Saint-Venant system for laminar shallow water: numerical validation. *Discrete Contin. Dyn. Syst.* B 89–102.

HAGER, W. H., BREMEN, K. & KAWAGOSHI, N. 1990 Classical hydraulic jump: length of roller. *J. Hydraul. Res., IAHR* **28** (5), 591–608.

JEFFREYS, H. J. 1925 The flow of water in an inclined channel of rectangular section. *Phil. Mag.* **49**, 793–807.

KAPITZA, P. L. & KAPITZA, S. P. 1949 Wave flow of thin layer of a viscous fluid. III. Experimental study of undulatory flow conditions. *Zh. Eksp. Teor. Fiz* **19**, 105. Also in *Collected Papers of P. L. Kapitza* (ed. D. Ter Haar), vol. 2, pp. 690–709. Pergamon, 1965.

https://doi.org/10.1017/jfm.2012.96 Published online by Cambridge University Press

KRANENBURG, C. 1992 On the evolution of roll waves. *J. Fluid Mech.* **245**, 249–261.

LAWRENCE, D. S. L. 1997 Macroscale surface roughness and frictional resistance in overland flow. *Earth Surf. Process. Landf.* **22**, 365–382.

LIU, J., JONATHAN, D. P. & GOLLUB, J. P. 1993 Measurements of the primary instabilities of film flows. *J. Fluid Mech.* **250**, 69–101.

MISRA, S. K., KIRBY, J. T., BROCCHINI, M., VERON, F., THOMAS, M. & KAMBHAMETTU, C. 2008 The mean and turbulent flow structure of a weak hydraulic jump. *Phys. Fluids* **20**, 035106.

NEEDHAM, D. J. & MERKIN, J. H. 1984 On roll waves down an open inclined channel. *Proc. R. Soc. Lond.* A **394**, 259–278.

NOBLE, P. 2006 On spectral stability of roll waves. *Indiana Univ. Math. J.* **55**, 795–848.

NOBLE, P. 2007 Linear stability of viscous roll waves. *Commun. Part. Diff. Equ.* **32** (10–12), 1691–1713.

PROKOPIOU, TH., CHENG, M. & CHANG, H.-C. 1991 Long waves on inclined films at high Reynolds number. *J. Fluid Mech.* **222**, 665–691.

RUYER-QUIL, C. & MANNEVILLE, P. 1998 Modeling film flows down inclined planes. *Eur. Phys. J.* B **6**, 277–292.

TESHUKOV, V. M. 2007 Gas-dynamics analogy for vortex free-boundary flows. *J. Appl. Mech. Tech. Phys.* **48** (3), 303–309.

THUAL, O. 2010 *Hydrodynamique de l'environnement*. Editions de l'Ecole Polytechnique.

WHITHAM, G. B. 1974 *Linear and Nonlinear Waves*. Wiley.

YU, J. & KEVORKIAN, J. 1992 Nonlinear evolution of small disturbances into roll waves in an inclined open channel. *J. Fluid Mech.* **243**, 575–594.

ZEL'DOVICH, YA. B. & RAIZER, YU. P. 2001 *Physics of Shock Waves and High-Temperature Hydrodynamic Phenomena*. Dover.

https://doi.org/10.1017/jfm.2012.96 Published online by Cambridge University Press